Chemical Engineering Journal xxx (xxxx) xxx

Contents lists available at ScienceDirect

Chemical Engineering Journal

journal homepage: www.elsevier.com/locate/cej

Bimetallic (Pt-Ni) La-hexaaluminate catalysts obtained from aluminum saline slags for the dry reforming of methane

J.J. Torrez-Herrera, S.A. Korili, A. Gil *

INAMAT˜2-Departamento de Ciencias, Edificio de los Acebos, Universidad Pública de Navarra, Campus de Arrosadía, E-31006 Pamplona, Spain

ARTICLE INFO

Keywords:
PtNi/La-hexaaluminate
Carbon dioxide
Methane
Temperature-programmed reduction
Electron microscopy

ABSTRACT

This work describes the synthesis of platinum-nickel/lanthanum hexaaluminates (PtNi/LHA) and their performance in terms of stability and catalytic activity in the dry reforming of methane (DRM) at 973 K. An Al solution (9.40 g/L) obtained from an Al saline slag waste by acid extraction was used to synthesize the hexaaluminate by mixing with a stoichiometric amount of lanthanum nitrate and methanol/Peg400/PegMn400 under hydrothermal conditions at 493 K for 16 h. After calcination at 1473 K for 2 h, the presence of LHA was confirmed. Wet impregnation of the synthesized support was used to obtain an initial Ni/LHA catalyst (10 wt% NiO) and the modified PtNi/LHA catalysts (0.2–1 wt% Pt). The support and catalysts were characterized by X-ray diffraction (XRD), N_2 adsorption at 77 K, temperature-programmed reduction (TPR), scanning electron microscopy (SEM) and transmission electron microscopy (HR-TEM). The analysis of the TPR patterns for the catalysts allowed the type of metal support interaction and NiO species to be determined, with a weak interaction with the support being observed in all cases. The presence of Pt promoted NiO reducibility. The PtNi/LHA catalysts synthesized were found to be active and very stable in the DRM reaction after reaction for 50 h. The catalytic behavior was evaluated from the CO_2 and CH_4 conversions, as well as the H_2/CO selectivity, with values of between 89% and 92% in almost all the time range evaluated. The presence of Pt improved the stability and catalytic performance of Ni/LHA thus improving resistance to coke formation.

1. Introduction

Global warming has driven the search for technological alternatives to mitigate its impact and thus avoid the increase in greenhouse gas emissions, with CO_2 and CH_4 representing an important part of the total quantity emitted into the atmosphere [1–4]. CO_2 is present naturally (in the ocean–atmosphere exchange, plant and animal respiration, soil decomposition, volcanic eruptions, etc.) and is also generated industrially. Similarly, at a global level, the main emission sources for CH_4 are the oil and natural gas industry, landfills, coal mines and biodigestive processes of organic matter (biogas) [5,6]. In 2015, as a consequence of this negative environmental scenario, 190 countries joined the United Nations Framework Convention on Climate Change (UNFCCC), which aims to limit global temperature rise to below 2 °C. Therefore, new strategies that will accomplish this goal are urgently required [5,7,8]. This new approach has allowed a developing technology, known as the dry reforming of methane (DRM), to gain greater momentum as this treatment can mitigate pollution and act as an important energy source, thus allowing the development of a comprehensive system for capturing greenhouse gases.

DRM is a highly endothermic reaction that is generally carried out at very high temperatures. As in any thermodynamic system, there are simultaneous reactions that compete with the main reaction. In this case, DRM (Eq. (1)) presents simultaneous reactions that affect the performance of this reforming technology, including CH_4 decomposition (Eq. (2)), the reverse water–gas shift reaction (RWGS) (Eq. (3)), the Boudouard reaction (Eq. (4)), CO_2 hydrogenation (Eq. (5)), CO hydrogenation (Eq. (6)) and steam reforming (Eq. (7)), respectively [9].

$$CH_4 + CO_2 \rightleftharpoons 2CO + 2H_2 \Delta H^0_{298K} = 247 kJ/mol \quad (1)$$

$$CH_4 \rightleftharpoons C + 2H_2 \Delta H^0_{298K} = 75.0 kJ/mol \quad (2)$$

$$CO_2 + H_2 \rightleftharpoons CO + H_2O \Delta H^0_{298K} = 41.0 kJ/mol \quad (3)$$

$$2CO \rightleftharpoons C + CO_2 \Delta H^0_{298K} = -173.0 kJ/mol \quad (4)$$

$$CO_2 + 2H_2 \rightleftharpoons C + 2H_2O \, \Delta H^0_{298K} = -90.0 kJ/mol \quad (5)$$

$$H_2 + CO \rightleftharpoons H_2O + C \Delta H^0_{298K} = -131.3 kJ/mol \quad (6)$$

$$CH_4 + H_2O \rightleftharpoons CO + 3H_2 \Delta H^0_{298K} = 206.3 kJ/mol \quad (7)$$

* Corresponding author.
E-mail address: andoni@unavarra.es (A. Gil).

https://doi.org/10.1016/j.cej.2021.133191
Received 20 September 2021; Received in revised form 17 October 2021; Accepted 22 October 2021
Available online 27 October 2021

Table 1
Chemical composition of the solution after acid extraction by ICP-OES.

Composition	Si	Al	Ca	Cu	Fe	K
g/L	0.33	9.40	1.19	0.090	1.03	0.081
Composition	Mg	Mn	Na	Ti	Zn	
g/L	0.36	0.058	0.12	0.042	0.18	

When using a stoichiometric ratio of CO_2 and CH_4, equal conversions should be obtained, thus leading to a synthesis gas ratio equal to 1. A H_2/CO ratio lower than 1 indicates that the dynamics of the system are being governed by Eq. (3). As such, equations (4) - (6) would be responsible for coke deposition on the catalyst [10]. The RWGS domain can be corroborated by the production of H_2O and also a higher conversion of CO_2 than of CH_4 ($[CO_2] \gg [CH_4]$). The Boudouard reaction is characterized by an increase in the CO produced, and an increase in the conversion of CH_4 over that of CO_2 is a consequence of the decomposition of CH_4 [1,11]. The RWGS reaction and the hydrogenation of CO_2 and CO are responsible for coking of the catalysts, thereby negatively affecting the metal active sites of the catalysts [10,12–15].

Developing efficient and accessible catalysts that allow DRM to be scaled up to an industrial scale is essential in the application of this technology for environmental mitigation. As the support plays a key role in the catalytic activity, it must, therefore, be carefully selected to allow full advantage to be taken of its textural and chemical properties—such as textural characteristics, thermal stability, redox properties, oxygen storage capacity and basicity of the surface. This allows the metal-support interaction to be improved and increases the dispersion of active metallic particles, thereby minimizing the systemic effects of C deposition [16,17]. Catalysts are made up of two main parts, namely the support and the active phase, the latter of which can be a metal or a mixture of metals (Ni, Co, Pt, Mn, Fe, Cu, Cr, etc.). Hexaaluminates are an excellent choice for DRM catalytic supports due to their thermal stability [12,18–20].

Hexaaluminates have a high resistance to thermal shock and exhibit high phase composition stability above 1873 K. The general formula for hexaaluminates is $AB_xAl_{12-x}O_{19}$, where AB represents a large cation such as Ba, La, Na, etc. and a transition (Co, Cu, Fe, Mn, Ni, etc.) or noble metal (Ir, Pd, Rh, Ru, etc.) [21–25]. These materials have various uses as catalysts for high temperature applications, superionic conductors and luminescent laser materials, ceramics and matrices for immobilization of radioactive elements, amongst others. Their main disadvantages include their low porosity and some structural defects.

Noble metals such as Pt, Ru and Ir have been used for decades in DRM, generally showing higher activity and better resistance to C deposition than Ni [26–28]. The use of bimetallic catalysts has expanded in recent years, thus allowing advantage to be taken of the synergy of the active phases and providing benefits to the catalyst and, therefore, its performance during DRM. Ni is one of the most widely used metals due to its availability and low cost compared with others such as Ru-Rh. The presence of Pt in Ni-based catalysts inhibits the global formation of C, in particular carbon nanotubes (CNT) or whisker C, as long as it is well distributed over the Ni particles. In addition, Pt promotes the relative Ni content and prevents the sintering of Ni, thus allowing a displacement of the reducible mass fractions, such as free metallic particles and/or

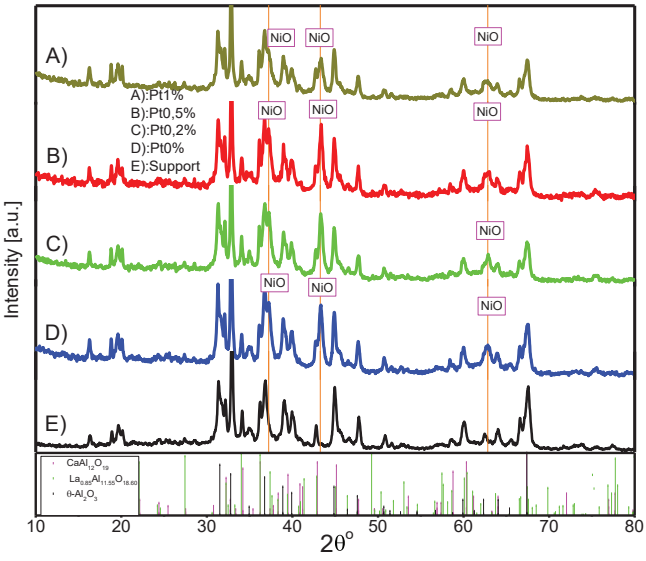

Fig. 1. XRD patterns of the Ni-Pt/hexaaluminates synthesized using La and Al extracted from saline slags (the hibonite and other patterns are included for comparison). A), B), C), D) correspond to 1, 0.5, 0.2, 0 wt% Pt with 10 wt% NiO on La-hexaaluminate); E) La-hexaaluminate support. Symbols: |Hibonite pattern #00–007-0785, |NiO pattern #01–073-1523, $La_{0.85}Al_{11.55}O_{18.60}$ #01–077-0338, |Θ-Al_2O_3 # 23–1009.

Table 4
BET specific surface areas, pore diameter and crystallite sizes for the samples synthesized.

Sample	S_{BET} (m^2/g)	dp (nm)		cristallite size (nm)
			LaHA	NiO (mean)
MPt4	45	39	35	13
MPt3	39	37		18
MPt2	43	40		17
MPt1	42	41		13

Table 2
Chemical composition of the saline slag before acid treatment by FRX.

Composition	Na_2O	MgO	Al_2O_3	SiO_2	P_2O_5	SO_3	Cl	K_2O	CaO
wt.%	8.65	2.76	41.71	4.23	0.05	0.52	11.83	4.40	2.08
Composition	TiO_2	Cr	MnO	Fe_2O_3	Ba	Cu	F	Zn	
wt.%	0.31	0.04	0.17	2.05	0.08	0.35	0.41	0.18	

Table 3
Chemical composition of the saline slag residue after Al extraction by FRX.

Composition	Na_2O	MgO	Al_2O_3	SiO_2	P_2O_5	SO_3	Cl	K_2O	CaO
wt.%	0.77	6.49	55.23	4.23	0.07	0.41	0.47	0.50	2.12
Composition	TiO_2	Cr	MnO	Fe_2O_3	Ba	Cu	F	Zn	
wt.%	0.65	0.07	0.26	1.25	0.07	0.51	0.41	0.17	

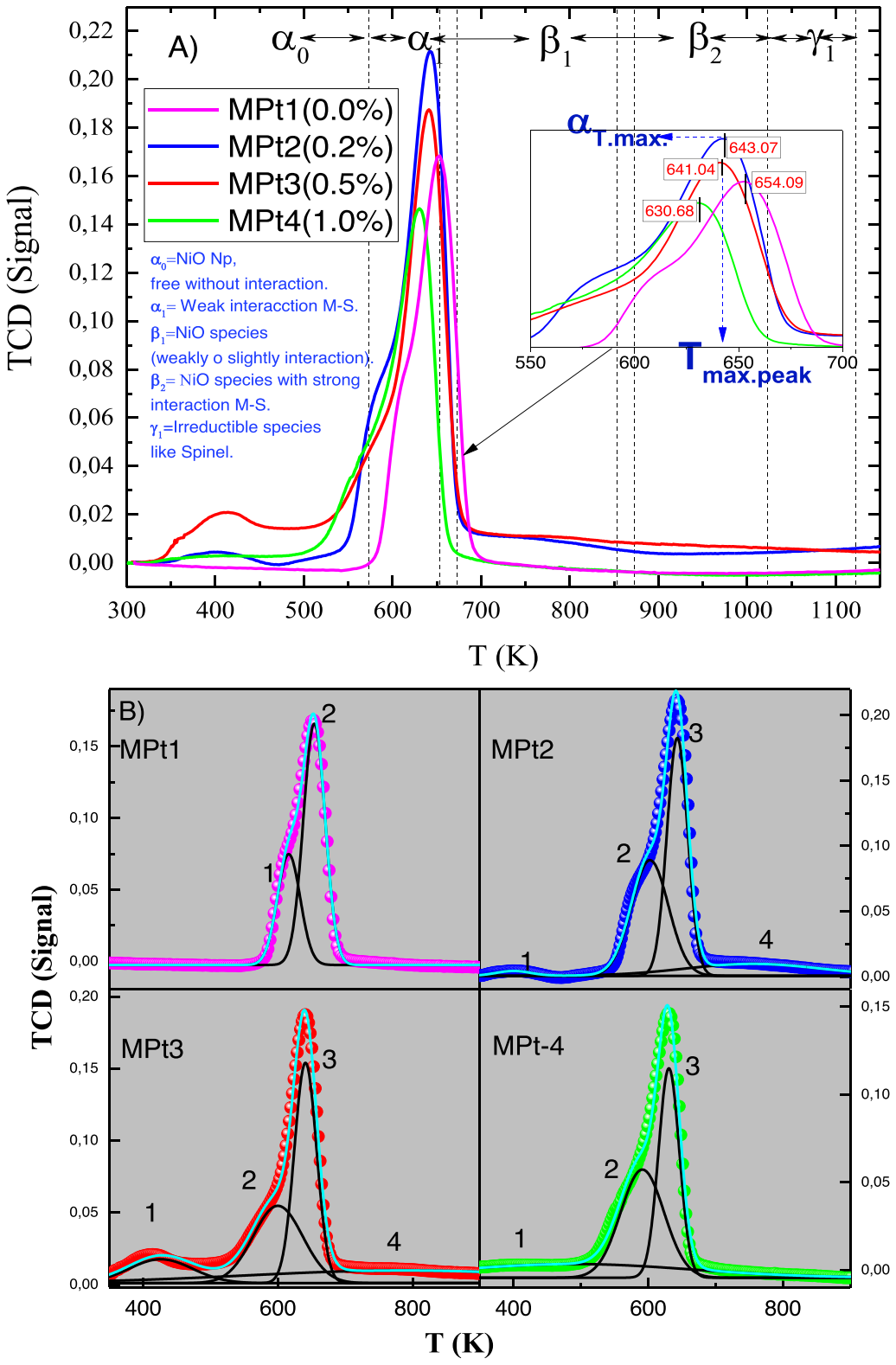

Fig. 2. A) TPR patterns of the Ni-Pt/hexaaluminate samples calcined at 1473 K. B) Peak deconvolution for MPt1 (0 wt% Pt), MPt2 (0.2 wt% Pt), MPt3 (0.5 wt% Pt), MPt4 (1 wt% Pt).

bimetallic grains of different sizes, at a lower temperature. Despite the high cost of Pt, small amounts of this metal are needed to obtain beneficial results and a reduction in the adsorption capacity of the CO produced, thus avoiding poisoning of the active sites and favoring the increase of H_2 [29–34]. Another important aspect arising from the addition of Pt to Ni is a substantial increase in the dispersion of Ni particles on the support. The morphology and type of C generated depends on the size of the Ni particles. Thus, larger particles generate filamentous C and smaller particles generate graphitic C. Depending on the interaction between the metals, it is possible to generate different core–shell structures, intermetallic alloys or monometallic heterostructures [29,35–37].

Table 5
Maximum temperature (T_{max}) and peak areas (A) of the TPR curves for the four PtNi/La-hexaaluminate catalysts.

Samples	Pt (wt.%)	T_{max} (K)	A (%)	peaks	Interacction type
MPt1	0.0	616	30.96	1	α
		654	69.04	2	
MPt2	0.2	400	1.53	1	α
		603	38.88	2	
		643	44.77	3	
		756	14.82	4	β_1
MPt3	0.5	426	10.59	1	α
		600	26.81	2	
		641	34.33	3	
		789	28.27	4	β_1
MPt4	1.0	484	24.01	1	α
		591	39.54	2	
		631	36.45	3	

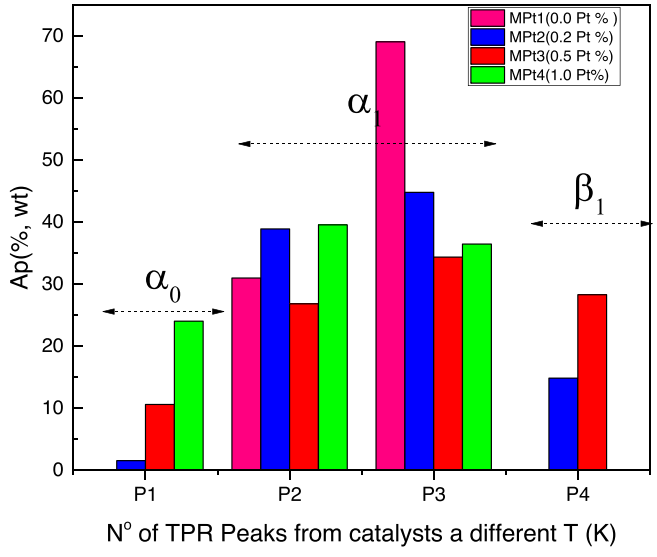

Fig. 3. Distribution of areas and interaction peaks for MPt1 (0 wt% Pt), MPt2 (0.2 wt% Pt), MPt3 (0.5 wt% Pt), MPt4 (1 wt% Pt).

Hexaaluminates have received particular attention in recent years and, as such, a number of different synthetic methods have been developed, including freeze drying, nitrate decomposition, solid-state reaction, C template, sol–gel, co-precipitation, reverse microemulsion, and hydrothermal synthesis, amongst others [38]. The most popular method for the synthesis of hexaaluminates is co-precipitation, in which the precursors are homogeneously mixed in the form of ions and precipitated simultaneously. Although significant efforts have been made in recent years to improve the textural properties of the synthesized materials using nonconventional drying methods and raw materials that enable technological scaling while lowering production costs, metallurgical slags could yet play a leading role [38].

During the recycling of secondary Al, wastes known as aluminum saline slags are generated. These slags contain metallic Al, various oxides and flux brines as main components, with variations in the percentage of non-metallic products depending on the nature of the material to be recycled [39–41]. This difference in composition makes it difficult to develop a standard recovery method and, at present, waste is mainly stored in controlled landfills. Due to their difficult final disposal, these slags have been used recently to synthesize several materials, including alumina [42–45], calcium aluminate [46–48], layered double hydroxides [49–54], microporous aluminophosphate molecular sieves [55,56], zeolites [57–62], pillared clays [63] and hexaaluminates [64,65]. Motivated by the need to find efficient environmental solutions that combine different technological stages, we have recently combined greenhouse gases with industrial waste to produce fuel. In this work, we continue with the development of bimetallic PtNi/La-hexaaluminate-based catalysts in order to valorize a high-impact industrial waste derived from the secondary Al manufacturing industry, evaluating its structure, activity and stability in DRM over a reaction period of at least 50 h.

2. Experimental

2.1. Materials, reagents and gases

Lanthanum(III) chloride heptahydrate (99.9%, Sigma-Aldrich), nickel(II) nitrate hexahydrate (99% Panreac), polyethylene glycol 400 (Merck), polyethylene glycol monolaurate 400 (PegMn400, Aldrich), methanol (99.8%, ACS) and diamminedinitritoplatinum(II) (Pt $(NH_3)_2(NO_2)_2$) 5 wt% solution in dilute ammonium hydroxide were used as materials and reagents for the synthesis of hexaaluminates and supported catalysts. CO_2 (99.996%, Praxair), He (99.999%, Praxair), H (99.999%, Praxair), CH_4 (99.5%, Praxair) and N (99.999%, Praxair) were also used in the characterization and catalytic performance studies.

Al was extracted from saline slags using the following procedure: 50 g of saline slag was added to 750 mL of an aqueous reagent solution (HCl 2 mol/L) in a reflux system consisting of a 1000 mL Erlenmeyer flask with tube condenser, thus avoiding volume losses. The slurries were heated to 373 K and kept at that temperature for 2 h. The solution was then allowed to cool and separated by centrifugation. The most important constituents of the filtered solution were determined by ICP-OES, using a VARIAN ICP-OES VISTA MPX with radial vision. The results obtained are summarized in Table 1. The composition of the separated powder before and after acid extraction was determined semi-quantitatively by X-ray fluorescence (XRF) using a PANalytical AXIOS instrument (see Table 2 and 3, respectively).

The synthesis of La-hexaaluminate-support was performed with a La/Al molar ratio of 1:11 using a previously reported method [64,65]. The slag solution was concentrated to one third of its initial volume to obtain a yellow liquor. A microemulsion was then prepared using methanol/Peg400/PegMn400/Al solution in a volumetric ratio of 1/0.8/0.4/0.6. Thus, lanthanum chloride was added to the Al solution at 353 K, under vigorous stirring. After 10 min, the methanol was added slowly, maintaining stirring for 10 min, then the Peg400 and PegMn400 were added and the temperature was increased to 373 K, maintaining the mixture under these conditions for 20 min prior to digestion in the autoclave. The resulting final mixture was heated in a stainless steel autoclave at 493 K for 16 h, dried in an oven until the liquid matrix had been eliminated, then calcined at 673 K for 1 h and 1473 K for 2 h, in both cases with a heating ramp of 10 K/min.

Wet impregnation of the La-hexaaluminate support synthesized was performed using 10 wt% of NiO and various loadings of Pt (0.2, 0.5, 1 wt %). The catalyst with the impregnated metallic phase was subsequently calcined at 673 K for 2 h. Four samples, denoted as MPt1, MPt2, MPt3, MPt4, corresponding to 0, 0.2, 0.5, 1 wt% Pt, respectively, were obtained.

2.2. Characterization techniques

The structural phases were analyzed using an X-ray diffractometer (model Siemens D5000) equipped with an Ni-filtered CuKα radiation source ($\lambda = 0.1548$ nm). The crystallite size was determined from the experimental diffractograms using the Debye–Scherrer equation. The main textural properties of the solids were determined by N adsorption at 77 K using a Micromeritics ASAP 2020 Plus adsorption analyzer. Prior to the adsorption measurements, 0.3 g of sample was degassed at 473 K for 2 h at pressures lower than 0.133 Pa. The BET surface area (S_{BET}) was calculated from adsorption data obtained over the relative pressure range 0.05–0.20. The total pore volume (V_P) was calculated from the

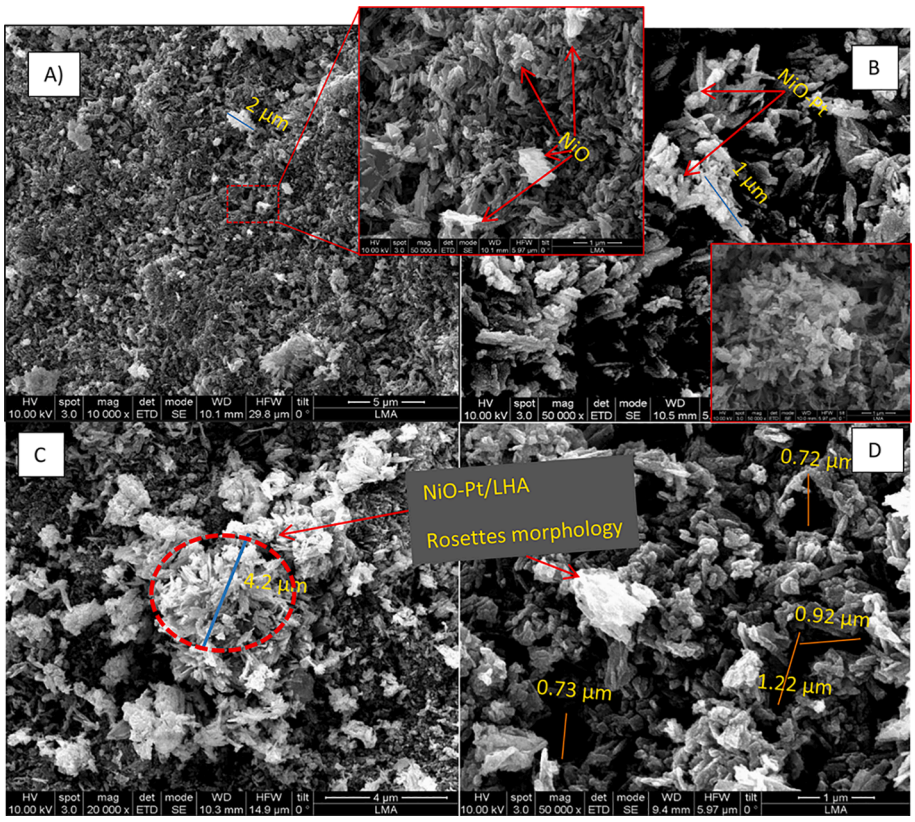

Fig. 4. SEM images of the catalysts calcined at 1473 K. A), B), C), D) correspond to MPt1, MPt2, MPt3 and MPt4, respectively.

amount of Ni adsorbed at a relative pressure of 0.99. Temperature-programmed reduction (TPR) studies were performed using a Micromeritics TPR/TPD 2900 equipment instrument. TPR tests were then performed from room temperature to 1273 K under a total flow of 30 mL/min (5% H_2 in Ar, Praxair). Finally, the morphological analysis and chemical composition of the samples were carried out by SEM (INSPECT F50, Mode: 30 kV - Map, Detector: BSD Full) and TEM (FEI Tecnai F30, Accelerating voltage: 200 kV, Detector: HAADF-STEM).

2.3. Catalytic performance

DRM was carried out at 973 K using an automated bench-scale catalytic unit (Microactivity Reference, PID Eng&Tech). The reactor was a tubular, fixed-bed, downflow type, with an internal diameter of 0.9 cm and a length of 30 cm. Catalyst samples (25 mg) were mixed with an inert material (SiC, VWV Chemicals-Prolabo) to dilute the catalyst bed and avoid hot-spot formation. The reaction mixture consisted of CH_4 and CO_2 with a molar ratio of 1:1 (concentration of 12% in the feed), with He as equilibrium gas up to a total feed flow of 40 mL/min, thus achieving a gas high spatial velocity (GHSV) of $9.6{\cdot}10^4$ mL/g h. Before the reaction, the catalyst was reduced *in situ* using 30 mL/min of H_2 at 973 K for 2 h. The reagent and product streams were analyzed using an Agilent 6890 gas chromatography system.

3. Results and discussion

3.1. Catalyst characterization

The X-ray diffractograms of the hexaaluminate catalysts synthesized using different Pt loads (0, 0.2, 0.5 and 1.0 wt%) and 10 wt% NiO are summarized in Fig. 1, comparing them with the support with no active phase. The support was calcined at 1473 K for 2 h and the catalysts with Pt-Ni were obtained by wet impregnation and calcined at 673 K for 2 h. The maximum peak of the diffractograms was at about 32.7° (2θ). The structure and size of the crystals were not affected by the subsequent impregnation of Pt-Ni, since the catalysts present the same crystallographic profile, namely that of the support together with peaks corresponding to NiO. The presence of NiO grains on La-hexaaluminate can be observed in A), B), and C), with peaks at 37.22°, 43.25° and 62.83° (2θ), respectively. The NiO peaks are intense, well-defined and very homogeneous in all samples and coincide with the NiO pattern # 01–073-1523. No peaks for Pt (metal or oxides) are observed in any of the samples. There may be several causes that justify these results. On the one hand, the low amount of incorporated Pt can make it not detectable by XRD, that it is not deposited forming crystals (they present an amorphous form) or that it is in a very dispersed form (very small crystals) not sensitive to the technique. Additionally, it is important to note that in the 2θ (°) positions corresponding to the Pt pattern (# 65–2868 and similar ones), 39. 75, 46.23, 67.45, there are peaks of defined intensity of the hexaaluminate support, superimposing the positions where they would be found the Pt grains detectable during the XRD measurements, thus not observing changes in these bands of the catalysts and the support.

The textural properties of the catalysts and the support, specific surface area (S_{BET}), pore diameter (pd) and crystallite size are presented in Table 4. The average crystallite size, as obtained using the Debye–-Scherrer equation, is 15.15 nm, with an S_{BET} of 43 m^2/g. It is important to note that the impregnation of NiO and the different Pt loads do not significantly reduce the specific surface area.

If a stream of reducing gas (H_2/Ar) is passed through the metal catalyst as the temperature is increased, the TPR analysis, it can provide qualitative information about the interaction between the active metallic phases and the support. There are various degrees of reduction closely linked to the MO-Al interaction force. The degrees of reduction of metallic oxides can be classified into four different types: α, β_1, β_2 and γ, depending on their level of interaction and range of reduction temperature. In the case of the reduction of NiO species, the α type corresponds to NiO species that interact weakly with the hexaaluminate support

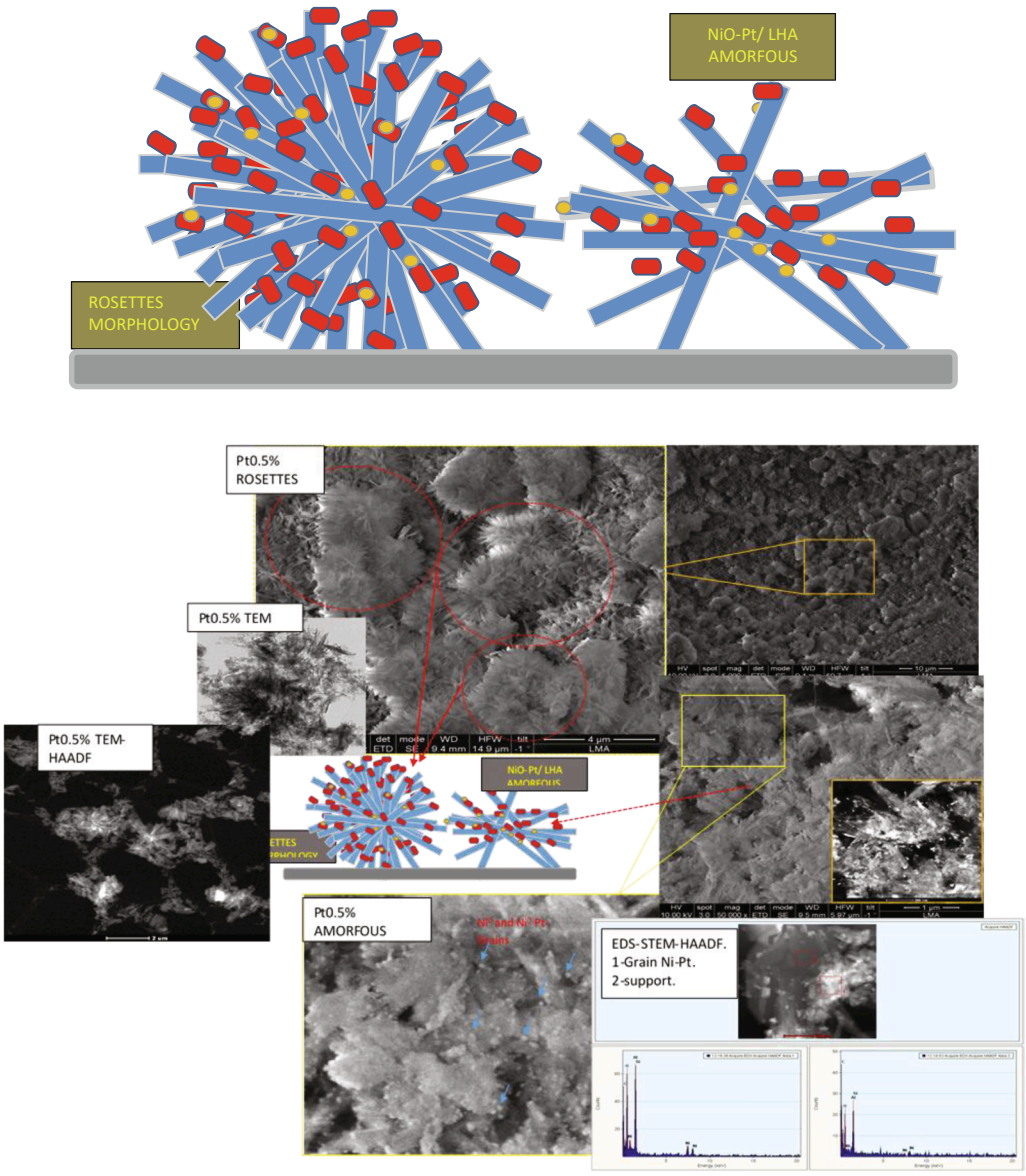

Fig. 5. Schematic representation of the catalyst morphology before the DRM stability test.

(573–673 K, free NiO species); β_1 corresponds to NiO species (reduction range 673–873 K, Ni rich in mixed-oxide phase), thus showing a soft or slight interaction with the support; β_2 corresponds to the NiO species with a strong oxide/support interaction (873–1023 K), which are therefore less reducible than the previous ones; and finally, the γ type belongs to the much less reducible NiO in the nickel aluminate phase with the spinel structure, with a reduction band in the range 1023–1123 K [66–69]. The addition of Pt to the catalysts generates a marked reducibility effect, which causes a decrease in the reduction temperature of the Ni while also providing resistance and improving the activity of the catalyst [6,33,70,71]. Additionally, the TPR analyses could also allow the reduction mechanism to be identified and the activation energy, kinetic rate of reaction and the parameters that determine its behavior to be determined. In the same way, the morphology in which the grains of the active phase grow during reduction could also be predicted [65].

As no peak was found in the TPR analysis carried out for the support, the appearance of peaks during the catalyst-reduction process must be directly related to the reductive stages of the Pt-Ni metal species. The TPR patterns for the different La-hexaaluminate samples, with their respective Pt-Ni loads (10 wt% NiO and 0, 0.2, 0.5, 1 wt% Pt), can be found in Fig. 2. The superposition of the TCD curves, which show the reduction behavior of the impregnated species, is shown in Fig. 2 A). MPt1 shows a maximum peak at 654 K, followed by MPt2 (653 K), MPt3 (641 K) and MPt4 (640 K). We can also see a decreasing displacement in the maximum peak reduction temperature with an increase in wt.% Pt, with a slope - ΔT_{max} of approximately 23 K, as well as the effect that this has on the morphology of the sintered Ni grains. This can be seen from the appearance of other peaks in the samples containing Pt, which are more or less available for reduction depending on the shape adopted during their growth. It is important to note that the curves show different reduction behaviors, although the highest reduction fraction is in the range of mild/weak α-type interactions characteristic of the reduction of metallic oxides. Fig. 2 B) and Table 5 show the deconvolution of the TCD curves for all samples synthesized and the data obtained from the TPR analysis, including peak area (A), maximum peak temperature (T_{max}) and type of interaction. MPt1 exhibits two peaks from the deconvolution with reduction values of $T_{max} \approx 616$ and 654 K and a maximum peak area percentage (A_{max}) of 30.96% and 69.09% for P1 and P2, respectively. The deconvolution allows us to assign two types of interaction α, α_0 and α_1, based on the maximum reduction temperatures. P1 falls in the middle of the α interaction region whereas P2 type

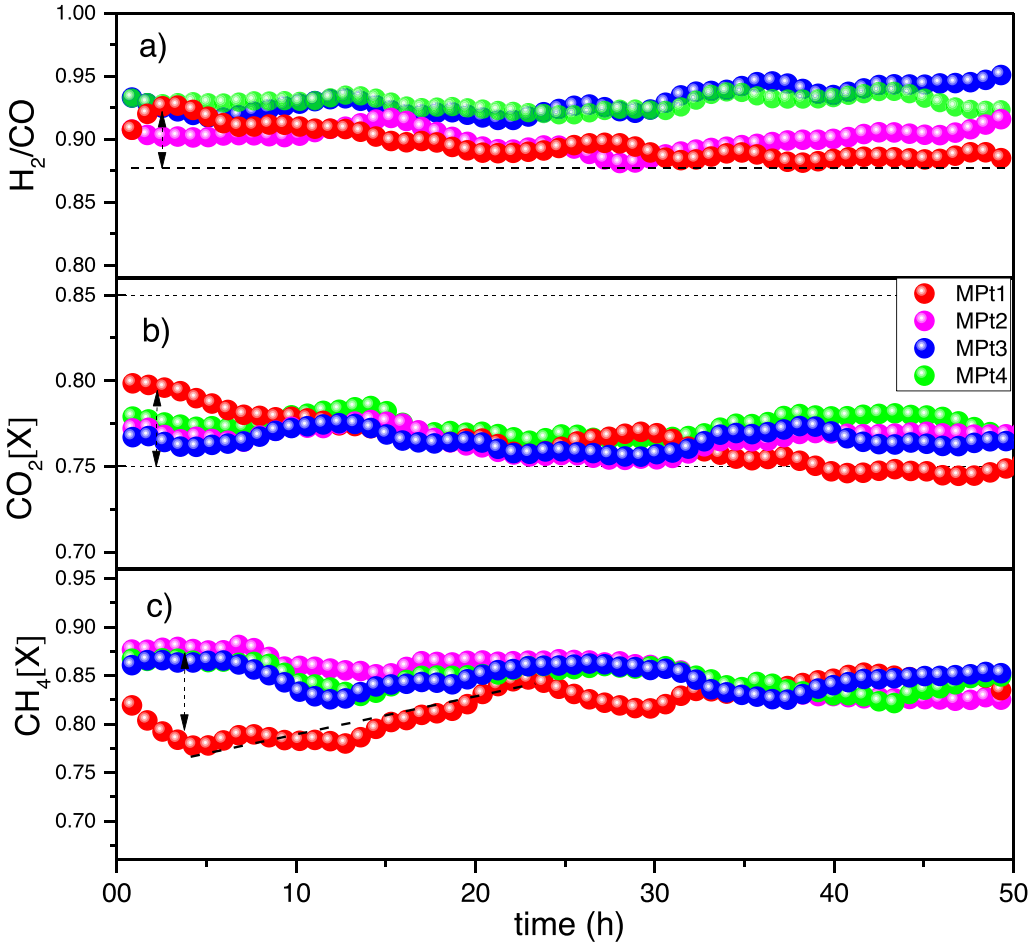

Fig. 6. Stability of the catalysts at 973 K for 50 h. a) H_2/CO selectivity. b) CO_2 conversion. c) CH_4 conversion.

appears at the α-β_1 transition region, therefore the largest fraction (69.09%, P2) of reduced Ni species presents a slightly greater interaction than P1 (free particles), with a high presence of mixed oxides. Four different peaks are seen for MPt2 (T_{max} ≈ 400, 603, 643, 756 K, with areas of A ≈ 1.53, 38.88, 44.77, 14.82%, respectively). As such, 82% of the Pt-Ni grains present a weak interaction (α), 15% present an interaction corresponding to mixed oxides (β_1), and an α_0 interaction corresponding to free Pt-Ni nanoparticles/grains with practically zero interaction represents a very low and insignificant percentage of the total active phase (1.53%). Therefore, the addition of Pt directly affects the NiO reduction profile, resulting in a greater distribution of these particles on the support and slightly reducing the interaction of a larger fraction, although this represents a smaller mass fraction with a greater interaction with respect to MPt1. Four characteristic peaks are also found for MPt3, in the range T_{max} ≈ 426–789 K, with area distributions for peaks 1–4 of A ≈ 10.59%, 26.81%, 34.33%, and 28.27%, respectively. In this case we can also observe a more uniform distribution of the mass fractions, with a marked displacement in both directions. Thus, approximately 60% of nanoparticles exhibit a low or slight interaction of free species and around 10% practically no interaction with the support. An increase to around 29% of β_1 (Pt-NiO rich in mixed oxides) is also seen. If we compare this distribution (MPt3) with that found for MPt2, we can see that the increase in the amount of impregnated Pt results in an increase of 14% for the β_1-type (P3) interaction and 9% of particles exhibit almost zero interaction (P1 - α_0). This effect is also seen when comparing MPt1 with MPt2 with the appearance of a new peak at low temperature (see Fig. 2 B and Table 5). MPt4 presents an increase in the fraction of free nanoparticles with practically zero interaction (see Fig. 3) to 14% compared to MPt3, with the remaining 75% presenting a weak or slight interaction (type α_1). In this case, the increase in the fraction of nanoparticles with no interaction may have been caused by the 1% increase in Pt.

The distribution of the peak areas for the different Pt loads can be seen in Fig. 3. The sample containing no Pt (MPt1) exhibits only two overlapping peaks due to the effect of morphology and NiO grain size, and is characteristic of low/very weak interactions. As different percentages of Pt are added, the reduction profile shifts, with the appearance of peaks in the range of mixed oxides ($\beta_1 \gg \alpha_1$) and of very small and dispersed nanoparticles ($\ll \alpha_1$) that are easily attacked by H_2 at low temperatures (MPt2, MPt3). The distribution for MPt4 shows that the fraction corresponding to slight interaction remains essentially constant, with a significant increase in the amount of particles exhibiting no interaction. In the case of NiO reduction, we know that the appearance of different peaks is associated with different degrees of interaction but also with the presence of particles and grains of different sizes and morphologies, which either benefits or hinders the access of H_2 to all oxide particles present. It is clear that the addition of Pt exerts a dispersing effect on the NiO on the support and also affects the distribution of the mass fractions with different interactions.

The morphological aspects of the support and the metallic phase are of vital importance as regards understanding, assigning and correlating the catalytic performance of the catalysts with the porosity, shape, size, distribution and ordering of the different structures found in said materials. As such, SEM images for the synthesized catalysts are presented in Fig. 4, where A), B), C), and D) correspond to MPt1, MPt2, MPt3, and MPt4, respectively. All catalysts exhibit practically the same morphology, which is a mixture of clusters of agglomerated tables in the form of rosettes (Fig. 4 C)) and amorphous agglomerates with interstices

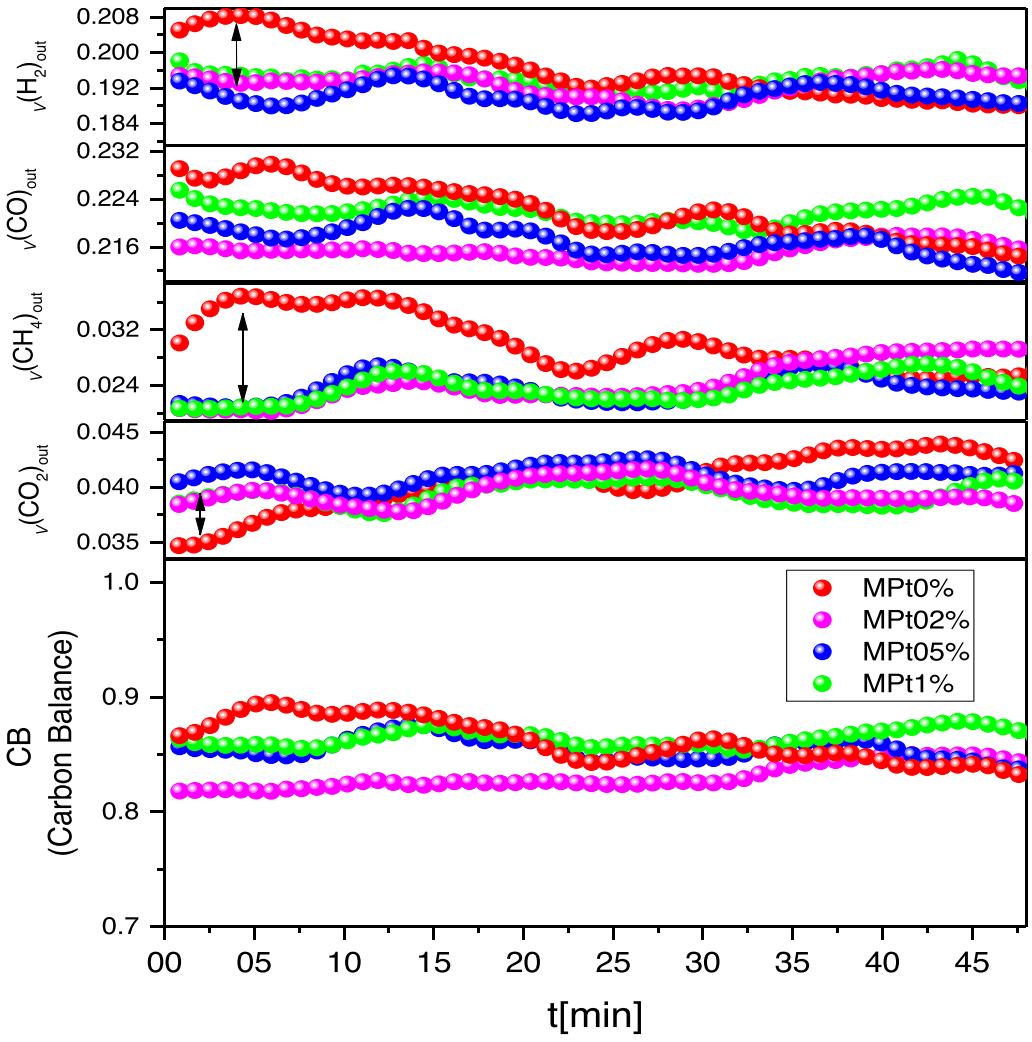

Fig. 7. Volumetric fraction of gases leaving the reactor (top: H_2, CO, CH_4, CO_2) and carbon balance (bottom: CB) for catalysts at 973 K for 50 h in the stability test.

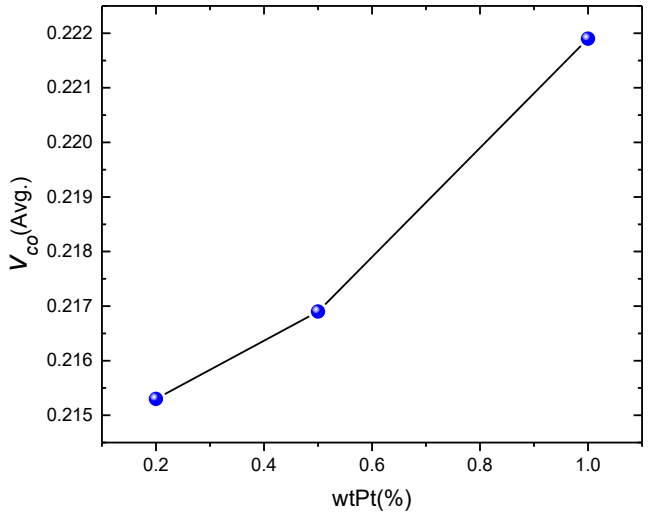

Fig. 8. Average volumetric fractions for MPt1-2–3 as a function of the weight load of Pt.

and a porosity of between 0.7 and 1.5 μm. The configuration of the rosette-shaped agglomerates increases the area available for the deposition of metals, thus resulting in a larger number of active sites and NiO-Pt nanoparticles that are not conditioned by the porosity. The rosette-type morphology presents a diameter of 4–10 μm and amorphous clusters of 1–4 μm. The schematic representation in Fig. 5 shows an example of the contribution of both morphologies in the distribution/dispersion of metals deposited on the surface of the support and how these allow an increase in the density of active sites.

3.2. Catalytic performance

Catalytic stability tests were carried out for the catalysts at 973 K for 50 h after reduction with 5% H_2/Ar for 2 h. The results obtained in the catalytic performance are presented in Fig. 6. Reactant conversion $[X]_i$, selectivity [H_2/CO], carbon balance (CB) and product yields (Y_{CO}·Y_{H2}) were calculated using the following equations (adapted to several authors [65,72–80]):

$$[X]_{CH_4} = \frac{[F_{CH_4}]_{in} - [F_{CH_4}]_{out}}{[F_{CH_4}]_{in}} \quad (1)$$

$$[X]_{CO_2} = \frac{[F_{CO_2}]_{in} - [F_{CO_2}]_{out}}{[F_{CO_2}]_{in}} \quad (2)$$

$$Y_{H_2} = \frac{[F_{H_2}]_{out}}{2^*[F_{CH_4}]_{in}} \quad (3)$$

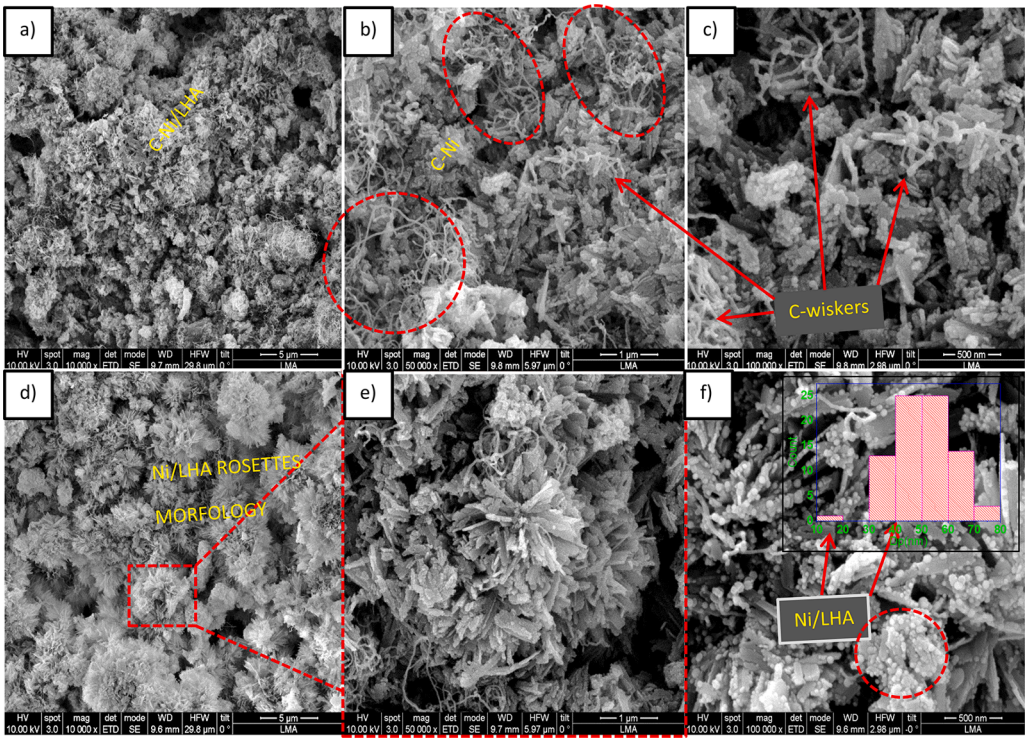

Fig. 9. SEM images for used MPt1 catalyst after DRM at 973 K for 50 h.

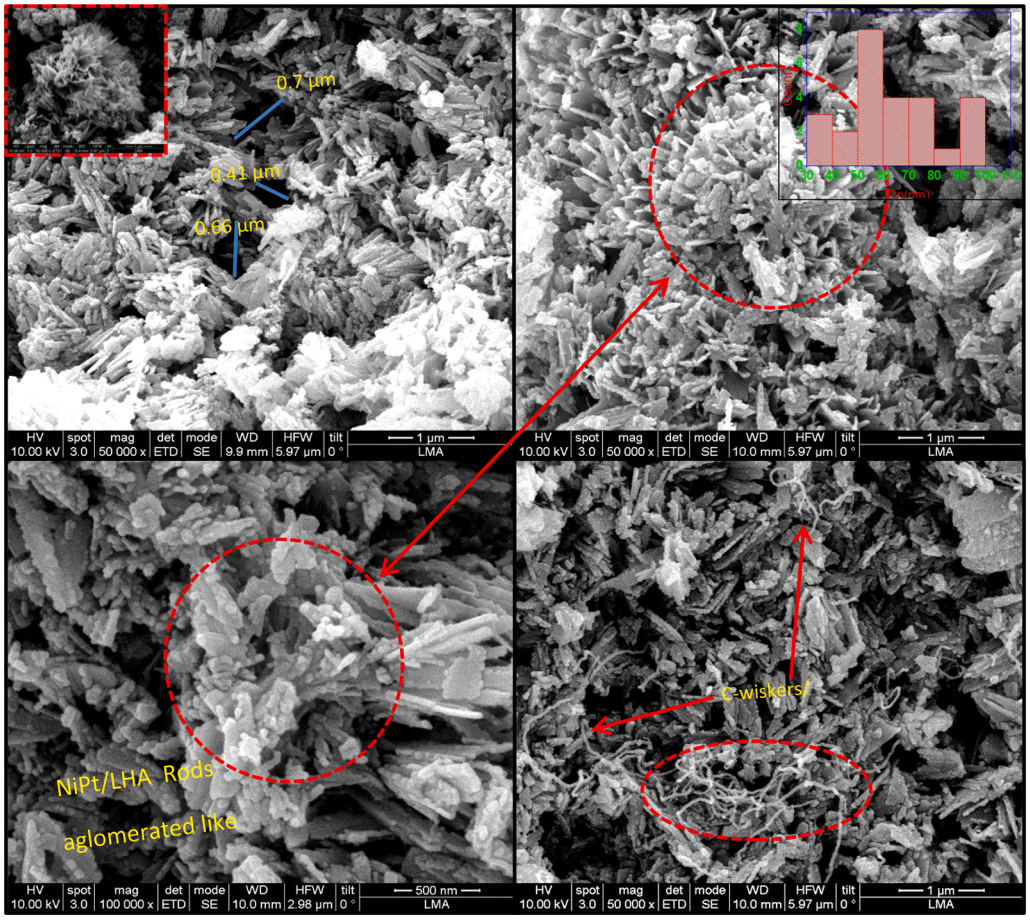

Fig. 10. SEM images for used MPt2 catalyst after DRM at 973 K for 50 h.

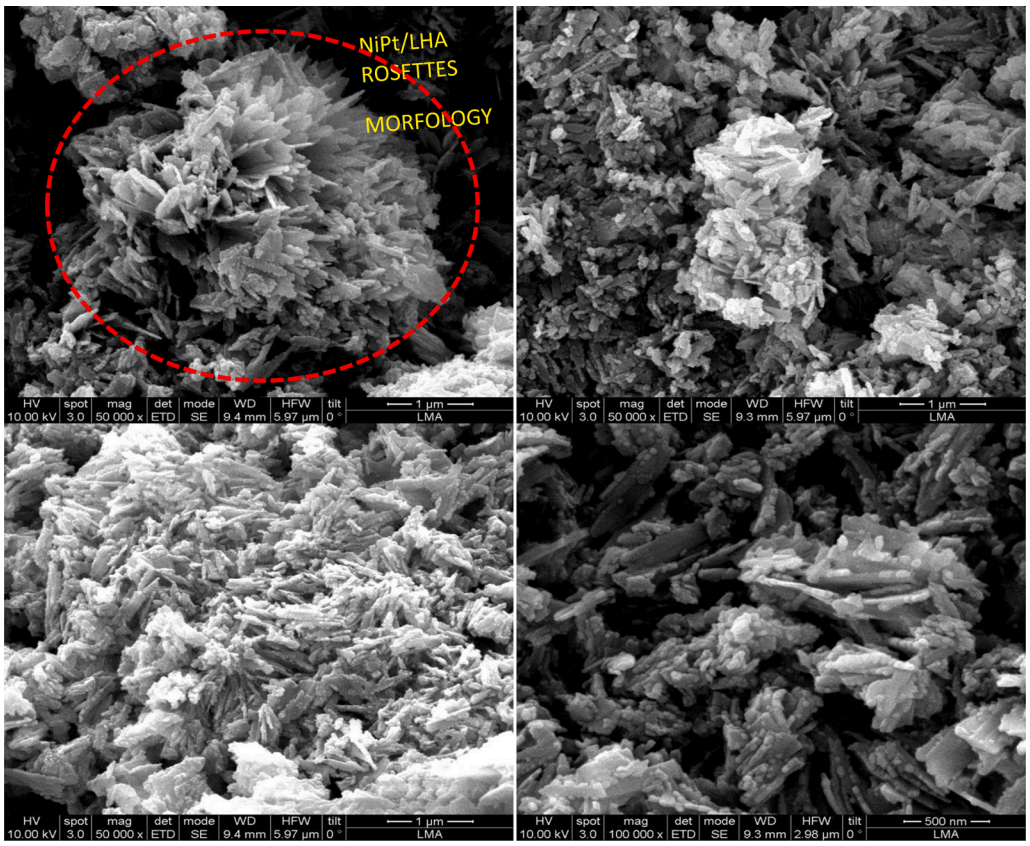

Fig. 11. SEM images for used MPt3 catalyst after DRM at 973 K for 50 h.

$$Y_{CO} = \frac{[F_{CO}]_{out}}{[F_{CH_4}]_{in} + [F_{CO_2}]_{in}} \tag{4}$$

$$\text{Selectivity}\left[\frac{H_2}{CO}\right] = \frac{Y_{H_2}}{Y_{CO}} \tag{5}$$

$$CB = \frac{[CO_2]_{out} + [CO]_{out} + [CH_4]_{out}}{[CH_4]_{in} + [CO_2]_{in}} \tag{6}$$

$$Volume fraction : v_i = \frac{V_i}{V_T} \tag{7}$$

Fig. 6 a) shows the selectivity values with respect to H_2 for the catalysts, with MPt4 exhibiting the most stable behavior over time, followed by MPt3, MPt2, and MPt1 ($X_{|H2/CO|}$ values ≈ 92%, 93%, 90% and 89%, respectively), in the same order that the Pt content decreases. MPt4 exhibits a small difference between the final and initial $\Delta X_{\frac{H_2}{CO}}$ values of −0.95%, thus indicating a slight decrease in the H_2/CO ratio at the end of the test. The other catalysts show a trend with fewer fluctuations (always around 93%), although with a slight decrease in the last five hours. MPt3 shows a very similar behavior to that of MPt4, but with a slight increase after 30 h of reaction and a $\Delta X_{\frac{H_2}{CO}}$ value of around 1.79%. MPt2 and MPt1 exhibit a decreasing selectivity until 30 h, as in the previous cases, after which the value for MPt2 begins to increase to resemble that for MPt3, with a final $\Delta X_{\frac{H_2}{CO}}$ of around 0.84%. In contrast to MPt2-3, the value for MPt1 continues to decrease, with a slope of $\Delta X_{\frac{H_2}{CO}}$ of around −4%, thus differing markedly from the rest of the samples, probably due to the absence of Pt. It should be remembered that the presence of Pt favors the reducibility of NiO as can be seen in the TPR analysis presented in Fig. 2. As such, it can be seen that a more stable behavior, in terms of the H_2/CO ratio, is obtained a function of the amount of Pt added to the catalyst. The CO_2 conversion (Fig. 6 b)) for MPt4-3–2 presents values of around 77%, with a very similar behavior between them, but different to that shown by MPt1, which starts with values of ≈ 80% conversion and ends with values of ≈ 74%. It should be noted that the conversion value for MPt4 is slightly higher than those for MPt3-2. As in the previous case, the conversion of CH_4 (Fig. 6 c)) maintains the similarities between the samples containing Pt and that without it. Thus, MPt4-3–2 present conversion values of around 87%, with a similar behavior, whereas MPt1 begins with a value of around 77% and ends with a value of around 82%, thus meaning that the conversion gradually increases from the initial stage of the reaction. This increase can be divided into two regimes: during the first 25 h the conversion increases with a slope of 7.9%, subsequently continuing up to 50 h with a value of 2.1%.

Fig. 7 shows the volumetric fractions for the different gases at the outlet of the reactor over 50 h for all catalysts, as well as the carbon balance. MPt1 (Fig. 7, top) presents a different thermodynamic mechanism from the rest of catalysts in terms of the production of H_2-CO and consumption of CH_4-CO_2, with slopes of $\Delta v_i = -1.08, -0.77, -0.70, 0.43\%$ for H_2, CO, CH_4 and CO_2, respectively. In other words, H_2-CO production starts at a much higher rate than for the other catalysts, subsequently decreasing over the course of the reaction, possibly due to deactivation of the active Ni centers as a result of C deposition, probably related to the acidity of the catalysts. This results in blocking of the active sites, thereby decreasing the catalytic performance. The type of C generated is not adequate and the quantity is not sufficient for the deactivation gradient on the catalyst. As the deactivation effect is only small, this C could be whisker—or filamentous—, which is less detrimental than other forms of carbonaceous deposits, such as graphitic C. The consumptions of CH_4 and CO_2 present opposite behaviors, with a high rate for CH_4 in the first 25 h that decreases as the reaction progresses, associated with low conversion or production of this gas in parallel reactions. In contrast, the rate for CO_2 is low in the initial stages (indicating high consumption) with a positive slope, thus indicating that consumption decreases or that overproduction occurs. In light of these results, the

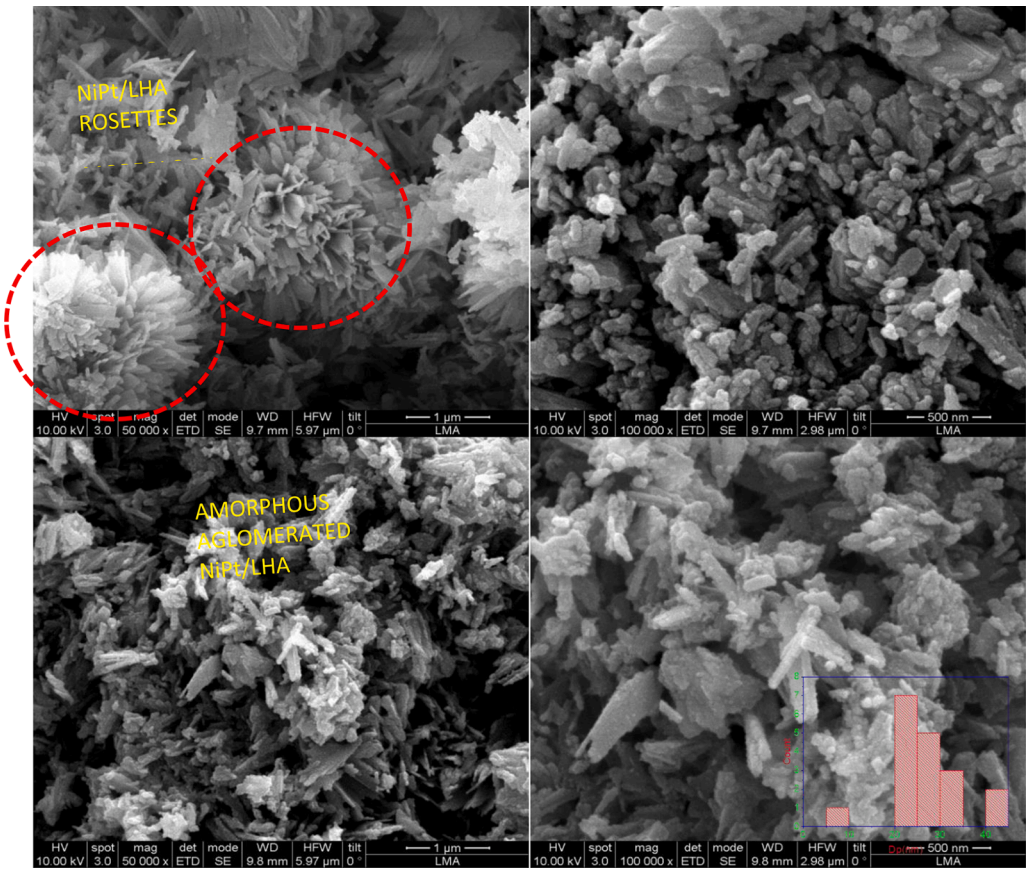

Fig. 12. SEM images for used MPt4 catalyst after DRM at 973 K for 50 h.

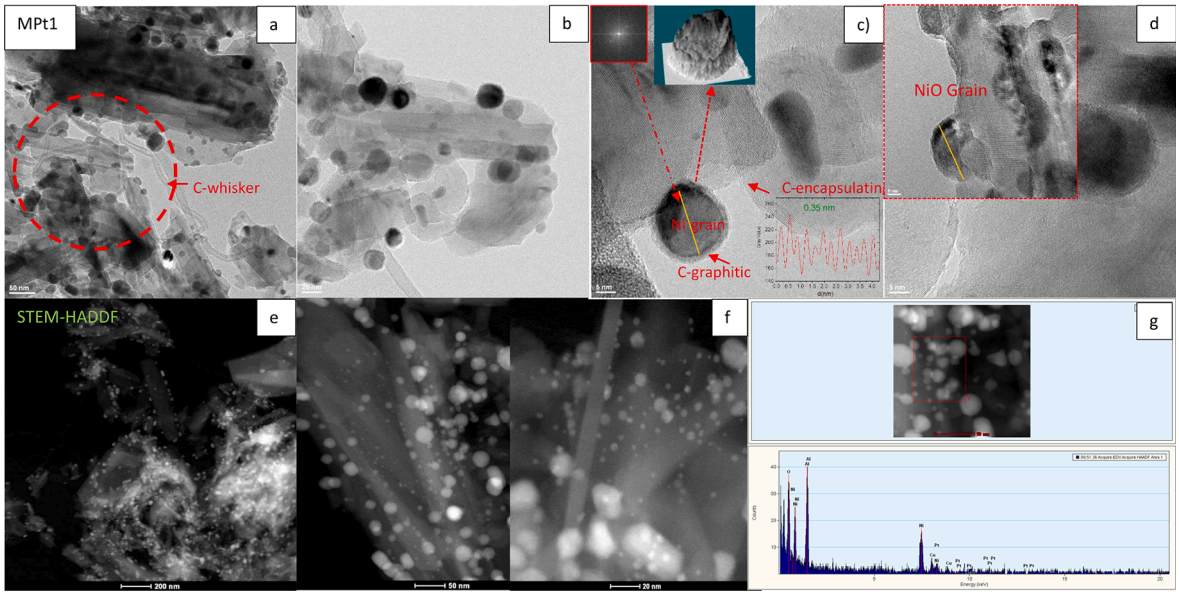

Fig. 13. HRTEM, STEM-HAADF and EDS images for used MPt1 catalyst after DRM at 973 K for 50 h.

dynamics of the system in the first 30 h of reaction is possibly governed by DRM, CO_2 methanation, and CH_4 decomposition, which would explain the high initial H_2-CO values, high CH_4 output (due to generation upon CO_2 methanation), and high consumption of CO_2, as well as the generation of C upon decomposition of CH_4. In the case of MPt2-3–4, we can see that the thermodynamic behavior at the outlet of the reactor is very similar for both products and reactants, with a slight increase in the magnitudes of V_{CO} for MPt4 with respect to MPt3-2 (see Fig. 8). We can also see that, as the Pt load increases, so does the average volumetric fraction, with values of $\overline{V_{CO}} = 0.222, 0.217, 0.215$ for MPt4, MPt3, and MPt2, respectively. With regard to the production of H_2 and consumption of CH_4-CO_2, these variables exhibit average values of $V_i = 0.194, 0.024, 0.040$ for H_2, CH_4, and CO_2, respectively, thus showing greater stability and better catalytic performance with the addition and increase of Pt as an aid to the catalytic reaction, most likely

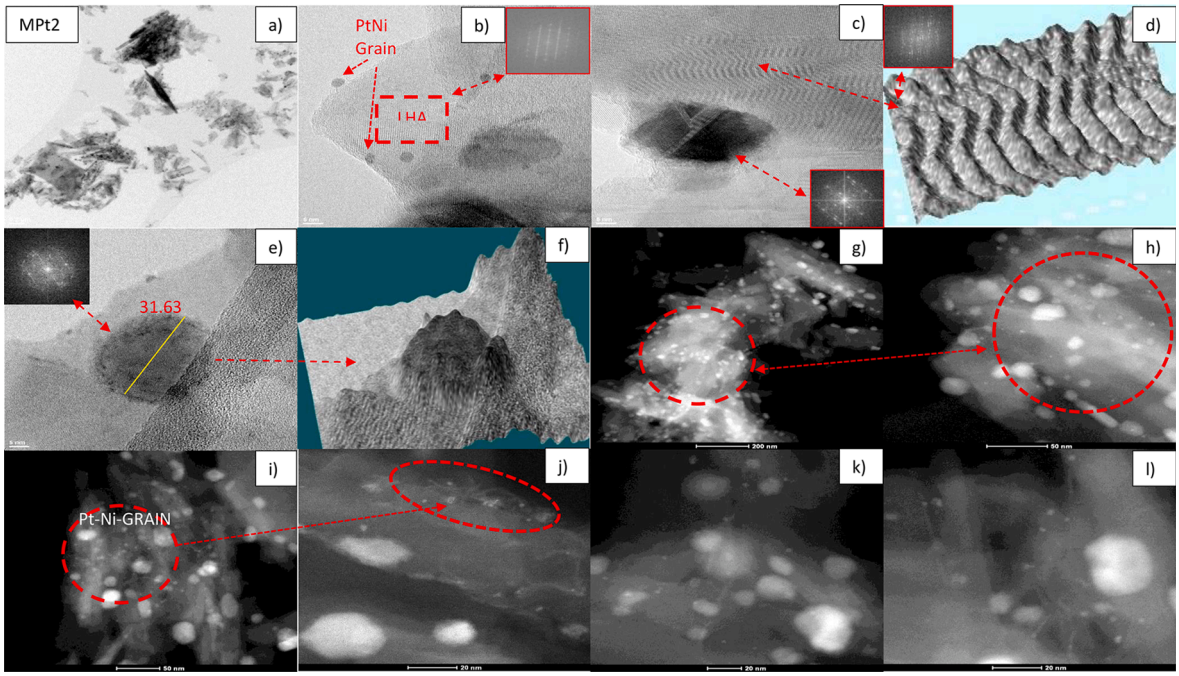

Fig. 14. TEM, STEM-HAADF and EDS images for used MPt2 catalyst after DRM at 973 K for 50 h.

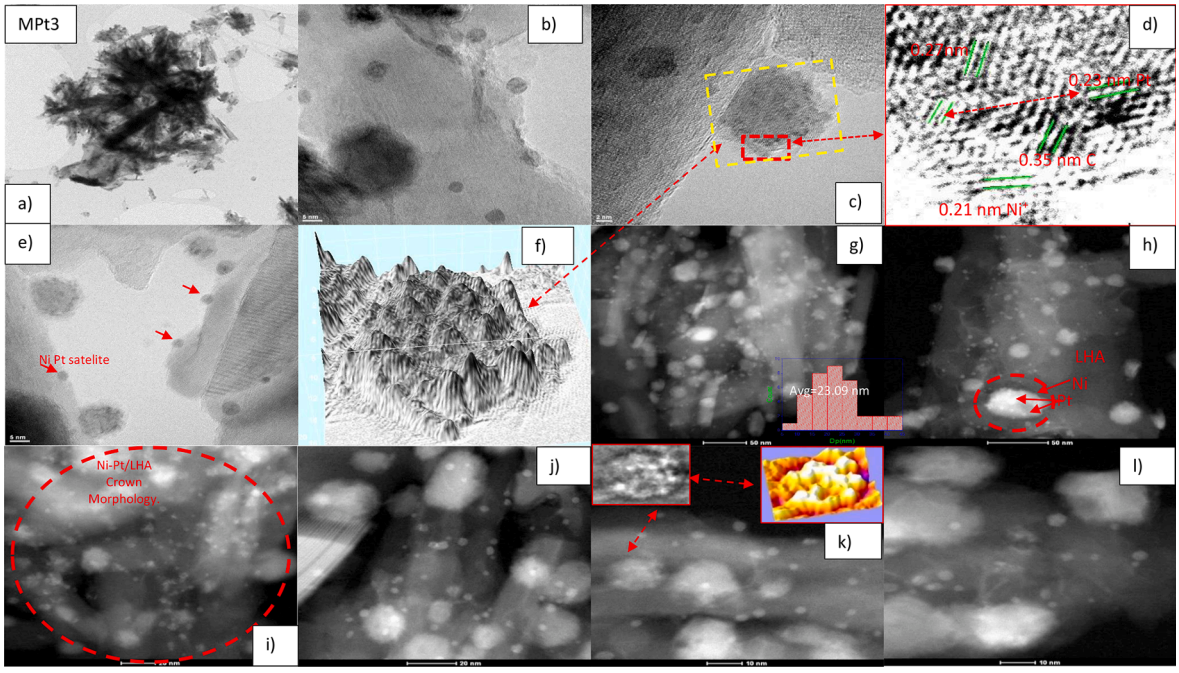

Fig. 15. TEM, STEM-HAADF and FFT images for used MPt3 catalyst after DRM at 973 K for 50 h.

due to the ease in reducing NiO due to the presence of Pt. As far as the carbon balance is concerned, the most stable behavior is presented by MPt4 (see Fig. 7 below), which exhibits an average value of 86.4%, with the least stable corresponding to MPt1, with a decreasing slope of −3.26%. It can be seen from Fig. 8 that the average volumetric fraction increases with Pt load, thus indicating that the addition of this metal decreases the adsorption of CO on the catalyst and improves the resistance to coking. [30–35].

3.2.1. SEM-TEM analysis of catalysts after catalytic tests

Fig. 9 shows the SEM images of MPt1 after 50 h of reaction in DRM at 973 K. The rosette-like morphology of the support can clearly be seen, along with clusters of tables (Fig. 9 a) d) e)), and amorphous agglomerates (Fig. 9 b) c)). C whiskers can also be seen in different regions of the catalyst. Fig. 9 f) shows the distribution of the reduced Ni particles on the agglomerates, amorphous tables and rosettes. In this case, about 70% of the agglomerated particles have a diameter of between 30 and 70 nm and a $\overline{dp} = 50.16nm$. Another important aspect is that there is a high particle density on the catalyst surface, which may be associated with a low metal support interaction and a high migration of nanoparticles due to thermokinetic effects, thus resulting in a size increase due to sintering of the Ni particles.

Fig. 10, which corresponds to MPt2, shows that the morphologies

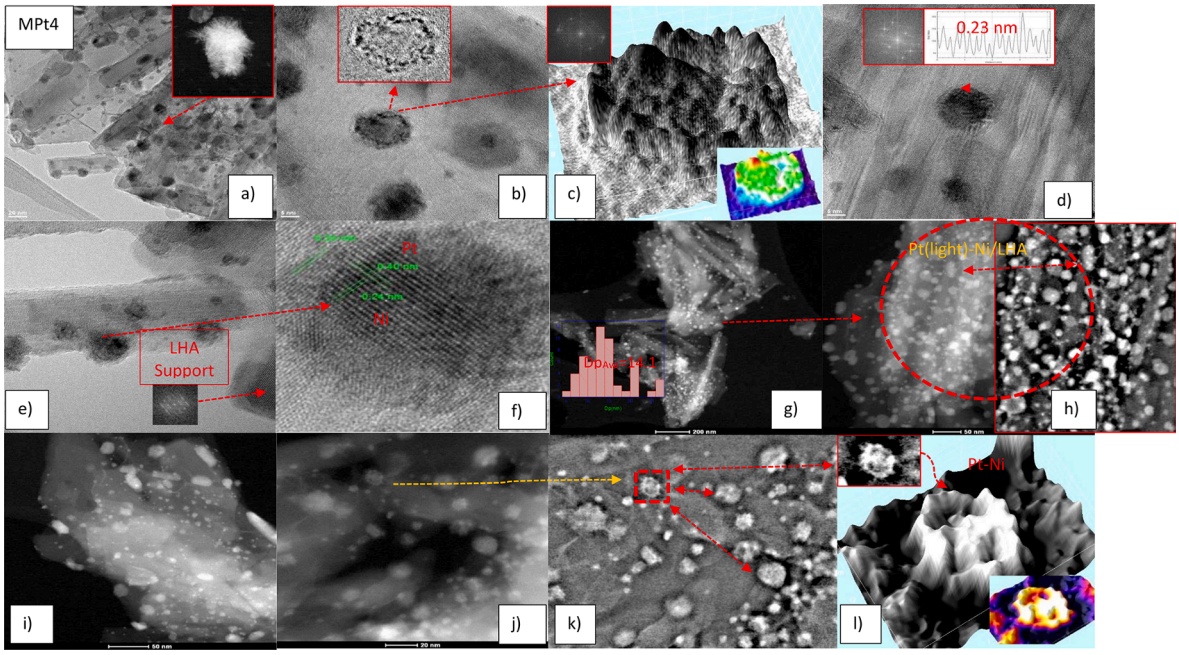

Fig. 16. TEM, STEM-HAAD, FFT and 3D images for used MPt4 catalyst after DRM at 973 K for 50 h.

identified for MPt1 are maintained, thus allowing Ni and Pt to be distributed over the rosettes and table clusters. In this case, the average diameter of the PtNi particles is 63 nm, with a distribution in which 70% of particles have an apparent diameter of between 40 and 80 nm, maintaining a quasi-spherical morphology. In addition, it can also be seen that, although some whisker C is present, there is much less than for MPt1, in other words CMPt2 ≪ CMPt1, possibly due to the addition of Pt. Although the quantity of Pt added is very small by weight compared to Ni, it appears to be sufficient to prevent a large increase in C deposition.

Fig. 11, which corresponds to MPt3, shows the absence of carbonaceous deposits for this catalyst. In this case $\overline{dp} = 49.31nm$ for PtNi, with more than 70% of nanoparticles in the range 30–70 nm, a very similar range to those found previously but with a much lower particle density than that found in MPt1. These particles are also more widely dispersed on the morphologies of the support (rosettes and clusters of amorphous tables), thus meaning that the effect of the increase in the amount of Pt, even suppressed but the formation of coke after 50 h in DRM, showing a behavior inversely proportional to the increase in Pt, that is, the greater the amount of Pt deposited, the lower the formation of coke.

In the case of MPt4, a decrease in the size of the PtNi particles, with a $\overline{dp} = 27.44nm$, corresponding to a distribution of between 20 and 30 nm for 80% of the particles, can be seen in Fig. 12. As in the case of MPt3, no coke deposits are observed on the metallic grains, thus corroborating the positive effect of adding Pt to the samples as regards the suppression of coke formation. The catalysts can be ordered as follows CMPt4 ≈ CMPt3 < CMPt2 ≪ CMPt1, which in turn indicates that the catalysts with the highest Pt content allow a better catalytic performance given their high resistance to deactivation by carbonaceous deposits. Another important aspect is that, despite the fact that the catalyst with no Pt presents the highest rate of carbonaceous deposition, this type of deposited C (whiskers) is the least detrimental in comparison with other forms, such as graphitic, pyrolytic and filamentous C, which are much more detrimental and more difficult to remove, therefore the cost-benefit ratio could be used determine whether Pt is used as an efficient suppressor of coke deposition or not.

The morphological analysis allows us to understand the effect of kinetic and thermodynamic phenomena on the catalyst during DRM and to identify the changes produced on the active phase (growth and size of crystals, deposition of detrimental products, blockages, textural properties, etc.). The HR-TEM (Fig. 13 a), b), c)) and STEM-HAADF images (Fig. 13 e), f)) for MPt1 are shown in Fig. 13. It can be seen that this catalyst, which lacks Pt, shows the presence of three types of C on the metallic phase, namely graphitic, filamentous (0.35 nm) and whisker C (Fig. 13 a), b), c)). In addition, the Ni grains present a $\overline{d_p} \approx 18.09nm$ as determined from the STEM-HAADF images, and the composition thereof is 7% Ni (Fig. 13 g)). This catalyst showed a higher deactivation rate as a result of the deposition of coke, which displaces the active metallic sites (whisker C) and blocks access to them by peripheral growth (graphitic and filamentous C). The box in Fig. 13 g) shows an image of MPt1 before the reduction-reaction step, with NiO grains with a diameter of 22 nm.

The TEM analysis, STEM-HAADF, fast Fourier transform (FFT) patterns and 3D images for MPt2 are shown in Fig. 14. The morphology of the amorphous clusters for the hexaaluminate support and their hexagonal FFT pattern (Fig. 14 a), b)) can clearly be seen. In addition, the PtNi grains and grooves are in accord to the FFT patterns, with this arrangement corresponding to Ni and the Pt nanoparticles on the Ni grains (Fig. 14 c), d), e)). Small quantities of graphitic C can also be seen on the surface of the metallic phase. The three-dimensional representation of the PtNi grooves and grains shown in Fig. 14 d) and f), where a crown-like formation of the reduced grains and grooves can be seen, provides information about the morphological growth of the particles. Moreover, the STEM-HAADF images (Fig. 14 g), h)) show the presence of Pt nanoparticles, which exhibit greater luminosity, on the metallic Ni grains. However, they are only seen in small quantities due to the low percentages deposited. Another aspect of importance is that essentially no C on the metallic surface, which could indicate an almost total suppression of coke deposition on the catalyst even with only a low dose of Pt (0.2 wt% Pt).

In the case of MPt3, the rosette-like morphology of the support, which benefits surface dispersion of the active phase, can be seen much more clearly (Fig. 15). The PtNi grains, with their respective lattice parameters of 0.21 nm Ni, 0.23 nm Pt and some graphitic-type C deposits (0.35 nm), are shown in Fig. 15 b), c), d), e). Fig. 15 f) shows a three-dimensional PtNi grain in which the crown shape can also be seen, as also corroborated by the STEM-HAADF images in Fig. 15 i), k). In addition, the distribution of Pt (brighter particles) on Ni agglomerates (Fig. 15 g), h), j), l)) is also shown, although with a higher presence of

crown-type grains than for MPt2. The mean size of the NiPt grains obtained upon image analysis was 23 nm. As noted previously, the suppression of C is almost total and is consistent with the results obtained in the catalytic test, which showed a high resistance to deactivation and, therefore, better performance than for MPt1-MPt2.

TEM and STEM-HAADF images for MPt4, as well as the FFT patterns and 3D images of the PtNi grains ($\overline{d_P} \approx 14.17nm$), are shown in Fig. 16. The rosette morphology of the hexaaluminate support and the deposited metal grains (Fig. 16 b), d)), with a Pt(1 0 0) lattice parameter of 0.23 nm, can be seen in the box of Fig. 16 a), along with the respective FFT patterns corresponding to NiPt nanoparticles. A 3D image of one of the grains from Fig. 16 b) is shown in Fig. 16 c). This allows us to corroborate the crown-like morphology of the metallic agglomerates on the support and the perfectly distributed arrangement of Pt (white points) on the rough surface of the Ni grains (dark region). The STEM-HAADF images show the presence of Pt nanoparticles on the Ni grains (more luminous particles in Fig. 16 g), h), i), j)), which maintain the crown-like morphology (Fig. 16 k), image taken using a band-pass filter). The amplified 3D image in Fig. 16 l) clearly shows the distribution of the PtNi grains. No carbonaceous deposits are observed, thus meaning that this catalyst is highly resistant to deactivation, with excellent stability and conversion at 973 K. In addition, although the thermodynamic behavior can be improved by increasing the temperature, the performance at this temperature is nevertheless excellent. It is therefore clear that the addition of Pt results in catalysts that are more resistant to deactivation since this additive suppresses coke deposition on the metallic particles, thus resulting in high stability and high conversions and a better metallic dispersion [35,36,81,82]. Crown-type grains could be associated with alloy-like morphologies in which Ni and Pt particles are either intertwined with each other in a dispersed manner or form small clusters [83–85].

4. Conclusions

PtNi/La-hexaaluminate bimetallic catalysts have been synthesized using an aluminum saline slag—a hazardous waste generated in Al recycling—as Al source in the synthesis of the La-hexaaluminate used as catalytic support. The catalysts were prepared by wet impregnation. A 10 wt% NiO catalyst was synthesized initially, then modified by incorporating various amounts of Pt (between 0 and 1 wt%), also by wet impregnation. This synthesis method generated two types of morphologies, namely rosettes and clusters of amorphous tables, which allowed an excellent distribution of the metallic nanoparticles on the support, as determined by SEM and HR-TEM.

The reduction temperatures of the NiO present in the Ni/LHA catalyst decreased due to the presence of Pt in the modified catalysts. In addition to the reducing effect, the addition of Pt generated high resistance to coke formation, thus resulting in a better performance of the catalyst in DRM. Indeed, the catalyst showed excellent stability after 50 h of reaction at 973 K. The conversion of CH_4 is higher than CO_2 and the H_2/CO selectivity is about 90%, thus suggesting the predominance of the Boudouard reaction over the RWGS reaction. The catalysts can be ordered as follows CMPt4 ≈ CMPt3 < CMPt2 ≪ CMPt1, which in turn indicates that the catalysts with the highest Pt content allow a better catalytic performance given their high resistance to deactivation by carbonaceous deposits. The combined analysis of SEM, HR-TEM and STEM-HAADF images also allows us to conclude that the presence of Pt reduces the size of the Ni particles, which may also be in accoed to the reduction in coke formation observed.

Declaration of Competing Interest

The authors declare that they have no known competing financial interests or personal relationships that could have appeared to influence the work reported in this paper.

Acknowledgements

The authors are grateful for financial support from the Spanish Ministry of Science and Innovation (MCIN/AEI/10.13039/501100011033) through project PID2020-112656RB-C21. JJTH thanks Universidad Pública de Navarra for a pre-doctoral grant. AG also thanks Santander Bank for funding via the Research Intensification Program.

References

[1] A. Abdulrasheed, A.A. Jalil, Y. Gambo, M. Ibrahim, H.U. Hambali, M.Y. Shahul Hamid, A review on catalyst development for dry reforming of methane to syngas: Recent advances, Renew. Sustain. Energy Rev. 108 (2019) 175–193, https://doi.org/10.1016/j.rser.2019.03.054.

[2] S.A. Cooper, K.K. Raman, J. Yin, Halo effect or fallen angel effect? Firm value consequences of greenhouse gas emissions and reputation for corporate social responsibility, J. Account. Public Policy 37 (3) (2018) 226–240, https://doi.org/10.1016/j.jaccpubpol.2018.04.003.

[3] C.D. Elvidge, M.D. Bazilian, M. Zhizhin, T. Ghosh, K. Baugh, F.-C. Hsu, The potential role of natural gas flaring in meeting greenhouse gas mitigation targets, Energy, Strateg. Rev. 20 (2018) 156–162, https://doi.org/10.1016/j.esr.2017.12.012.

[4] C. Song, Q. Liu, N. Ji, S. Deng, J. Zhao, Y. Li, Y. Song, H. Li, Alternative pathways for efficient CO_2 capture by hybrid processes—A review, Renew. Sustain. Energy Rev. 82 (2018) 215–231, https://doi.org/10.1016/j.rser.2017.09.040.

[5] O. Edenhofer, Climate change 2014: mitigation of climate change, Cambridge University Press, 2015.

[6] S. Arora, R. Prasad, An overview on dry reforming of methane: Strategies to reduce carbonaceous deactivation of catalysts, RSC Adv. 6 (110) (2016) 108668–108688, https://doi.org/10.1039/C6RA20450C.

[7] J. Rogelj, M. den Elzen, N. Höhne, T. Fransen, H. Fekete, H. Winkler, R. Schaeffer, F.u. Sha, K. Riahi, M. Meinshausen, Paris Agreement climate proposals need a boost to keep warming well below 2 °C, Nature 534 (7609) (2016) 631–639, https://doi.org/10.1038/nature18307.

[8] W.J. Jang, J.O. Shim, H.M. Kim, S.Y. Yoo, H.S. Roh, A review on dry reforming of methane in aspect of catalytic properties, Catal. Today 324 (2019) 15–26, https://doi.org/10.1016/j.cattod.2018.07.032.

[9] D.B. Pal, R. Chand, S.N. Upadhyay, P.K. Mishra, Performance of water gas shift reaction catalysts: A review, Renew. Sustain. Energy Rev. 93 (2018) 549–565, https://doi.org/10.1016/j.rser.2018.05.003.

[10] B. Abdullah, N.A. Abd Ghani, D.V.N. Vo, Recent advances in dry reforming of methane over Ni-based catalysts, J. Clean. Prod. 162 (2017) 170–185, https://doi.org/10.1016/j.jclepro.2017.05.176.

[11] A. Serrano-Lotina, L. Daza, Influence of the operating parameters over dry reforming of methane to syngas, Int. J. Hydrogen Energy 39 (8) (2014) 4089–4094, https://doi.org/10.1016/j.ijhydene.2013.05.135.

[12] M. Usman, W.M.A. Wan Daud, H.F. Abbas, Dry reforming of methane: Influence of process parameters—A review, Renew, Sustain. Energy Rev. 45 (2015) 710–744, https://doi.org/10.1016/j.rser.2015.02.026.

[13] Y. Kawashima, T. Handa, H. Takeuchi, M. Okumura, Effects of polyethylene glycol on the size of agglomerated crystals of phenytoin prepared by the spherical crystallization technique, Chem. Pharm. Bull. (Tokyo) 34 (8) (1986) 3403–3407, https://doi.org/10.1248/cpb.34.3403.

[14] T. Roussière, K.M. Schelkle, S. Titlbach, G. Wasserschaff, A. Milanov, G. Cox, E. Schwab, O. Deutschmann, L. Schulz, A. Jentys, J. Lercher, S.A. Schunk, Structure-activity relationships of nickel-hexaaluminates in reforming reactions Part I: controlling nickel nanoparticle growth and phase formation, ChemCatChem. 6 (2014) 1438–1446, https://doi.org/10.1002/cctc.201300960.

[15] G. Zhang, J. Liu, Y. Xu, Y. Sun, A review of CH_4 CO_2 reforming to synthesis gas over Ni-based catalysts in recent years (2010–2017), Int. J. Hydrogen Energy 43 (32) (2018) 15030–15054, https://doi.org/10.1016/j.ijhydene.2018.06.091.

[16] P. Frontera, A. Macario, A. Aloise, P.L. Antonucci, G. Giordano, J.B. Nagy, Effect of support surface on methane dry-reforming catalyst preparation, Catal. Today 218–219 (2013) 18–29, https://doi.org/10.1016/j.cattod.2013.04.029.

[17] N.A.K. Aramouni, J.G. Touma, B.A. Tarboush, J. Zeaiter, M.N. Ahmad, Catalyst design for dry reforming of methane: Analysis review, Renew. Sustain. Energy Rev. 82 (2018) 2570–2585, https://doi.org/10.1016/j.rser.2017.09.076.

[18] A.T. Ashcroft, A.K. Cheetham, M.L.H. Green, P.D.F. Vernon, Partial oxidation of methane to synthesis gas using carbon dioxide, Nature 352 (6332) (1991) 225–226, https://doi.org/10.1038/352225a0.

[19] J.T. Richardson, M. Garrait, J.K. Hung, Carbon dioxide reforming with Rh and Pt-Re catalysts dispersed on ceramic foam supports, Appl. Catal. A Gen. 255 (2003) 69–82, https://doi.org/10.1016/S0926-860X(03)00645-8.

[20] J.R. Rostrupnielsen, J.H.B. Hansen, CO_2-reforming of methane over transition metals, J. Catal. 144 (1) (1993) 38–49, https://doi.org/10.1006/jcat.1993.1312.

[21] S. Cimino, R. Nigro, U. Weidmann, R. Holzner, Catalytic combustion of methanol over La, Mn-hexaaluminate catalysts, Fuel Process. Technol. 133 (2015) 1–7, https://doi.org/10.1016/j.fuproc.2014.12.047.

[22] K.e. Zhang, G. Zhou, J. Li, K. Zhen, T. Cheng, Effective additives of A (Ce, Pr) in modified hexaaluminate $La_xA_{1-x}NiAl_{11}O_{19}$ for carbon dioxide reforming of methane, Catal. Letters 130 (1-2) (2009) 246–253, https://doi.org/10.1007/s10562-009-9876-3.

[23] T. Roussière, L. Schulz, K.M. Schelkle, G. Wasserschaff, A. Milanov, E. Schwab, O. Deutschmann, A. Jentys, J. Lercher, S.A. Schunk, Structure–activity relationships of nickel–hexaaluminates in reforming reactions Part II: activity and stability of nanostructured nickel–hexaaluminate-based catalysts in the dry reforming of methane, ChemCatChem. 6 (2014) 1447–1452, https://doi.org/10.1002/cctc.201300958.

[24] K. Ikkour, D. Sellam, A. Kiennemann, S. Tezkratt, O. Cherifi, Activity of Ni substituted Ca-La-hexaaluminate catalyst in dry reforming of methane, Catal. Letters 132 (1-2) (2009) 213–217, https://doi.org/10.1007/s10562-009-0094-9.

[25] M. Tian, X.D. Wang, T. Zhang, Hexaaluminates: a review of the structure, synthesis and catalytic performance, Catal, Sci. Technol. 6 (7) (2016) 1984–2004, https://doi.org/10.1039/C5CY02077H.

[26] C. Fan, Y.-A. Zhu, Y. Xu, Y. Zhou, X.-G. Zhou, D.e. Chen, Origin of synergistic effect over Ni-based bimetallic surfaces: A density functional theory study, J. Chem. Phys. 137 (1) (2012) 014703, https://doi.org/10.1063/1.4731811.

[27] Y. Khani, Z. Shariatinia, F. Bahadoran, High catalytic activity and stability of $ZnLaAlO_4$ supported Ni, Pt and Ru nanocatalysts applied in the dry, steam and combined dry-steam reforming of methane, Chem. Eng. J. 299 (2016) 353–366, https://doi.org/10.1016/j.cej.2016.04.108.

[28] Z. Bian, S. Das, M.H. Wai, P. Hongmanorom, S. Kawi, A review on bimetallic nickel-based catalysts for CO_2 reforming of methane, ChemPhysChem. 18 (22) (2017) 3117–3134, https://doi.org/10.1002/cphc.v18.2210.1002/cphc.201700529.

[29] I.V. Yentekakis, P. Panagiotopoulou, G. Artemakis, A review of recent efforts to promote dry reforming of methane (DRM) to syngas production via bimetallic catalyst formulations, Appl. Catal. B Environ. 296 (2021) 120210, https://doi.org/10.1016/j.apcatb.2021.120210.

[30] M. García-Diéguez, I.S. Pieta, M.C. Herrera, M.A. Larrubia, L.J. Alemany, Improved Pt-Ni nanocatalysts for dry reforming of methane, Appl. Catal. A Gen. 377 (1-2) (2010) 191–199, https://doi.org/10.1016/j.apcata.2010.01.038.

[31] T.D. Gould, M.M. Montemore, A.M. Lubers, L.D. Ellis, A.W. Weimer, J.L. Falconer, J.W. Medlin, Enhanced dry reforming of methane on Ni and Ni-Pt catalysts synthesized by atomic layer deposition, Appl. Catal. A Gen. 492 (2015) 107–116, https://doi.org/10.1016/j.apcata.2014.11.037.

[32] L. Li, L.u. Zhou, S. Ould-Chikh, D.H. Anjum, M.B. Kanoun, J. Scaranto, M. N. Hedhili, S. Khalid, P.V. Laveille, L. D'Souza, A. Clo, J.-M. Basset, Controlled surface segregation leads to efficient coke-resistant nickel/platinum bimetallic catalysts for the dry reforming of methane, ChemCatChem. 7 (5) (2015) 819–829, https://doi.org/10.1002/cctc.201402965.

[33] A. TANKSALE, J. BELTRAMINI, J. DUMESIC, G. LU, Effect of Pt and Pd promoter on Ni supported catalysts—A TPR/TPO/TPD and microcalorimetry study, J. Catal. 258 (2) (2008) 366–377, https://doi.org/10.1016/j.jcat.2008.06.024.

[34] G.W. Huber, J.W. Shabaker, S.T. Evans, J.A. Dumesic, Aqueous-phase reforming of ethylene glycol over supported Pt and Pd bimetallic catalysts, Appl. Catal. B Environ. 62 (3-4) (2006) 226–235, https://doi.org/10.1016/j.apcatb.2005.07.010.

[35] F. Meshkani, M. Rezaei, Nanocrystalline MgO supported nickel-based bimetallic catalysts for carbon dioxide reforming of methane, Int. J. Hydrogen Energy 35 (19) (2010) 10295–10301, https://doi.org/10.1016/j.ijhydene.2010.07.138.

[36] B. Pawelec, S. Damyanova, K. Arishtirova, J.L.G. Fierro, L. Petrov, Structural and surface features of PtNi catalysts for reforming of methane with CO_2, Appl. Catal. A Gen. 323 (2007) 188–201, https://doi.org/10.1016/j.apcata.2007.02.017.

[37] R. Ferrando, J. Jellinek, R.L. Johnston, Nanoalloys: from theory to applications of alloy clusters and nanoparticles, Chem. Rev. 108 (2008) 845–910, https://doi.org/10.1021/cr040090g.

[38] J.J. Torrez-Herrera, S.A. Korili, A. Gil, Progress in the synthesis and applications of hexaaluminate-based catalysts, Catal. Rev. (2020), https://doi.org/10.1080/01614940.2020.1831756.

[39] A. Gil, Management of the salt cake from secondary aluminum fusion processes, Ind. Eng. Chem. Res. 44 (23) (2005) 8852–8857, https://doi.org/10.1021/ie050835o.

[40] A. Gil, S.A. Korili, Management and valorization of aluminum saline slags: Current status and future trends, Chem. Eng. J. 289 (2016) 74–84, https://doi.org/10.1016/j.cej.2015.12.069.

[41] A. Gil, S. Albeniz, S.A. Korili, Valorization of the saline slags generated during secondary aluminium melting processes as adsorbents for the removal of heavy metal ions from aqueous solutions, Chem. Eng. J. 251 (2014) 43–50, https://doi.org/10.1016/j.cej.2014.04.056.

[42] B.R. Das, B. Dash, B.C. Tripathy, I.N. Bhattacharya, S.C. Das, Production of η-alumina from waste aluminium dross, Miner. Eng. 20 (3) (2007) 252–258, https://doi.org/10.1016/j.mineng.2006.09.002.

[43] B. Dash, B.R. Das, B.C. Tripathy, I.N. Bhattacharya, S.C. Das, Acid dissolution of alumina from waste aluminium dross, Hydrometallurgy 92 (1-2) (2008) 48–53, https://doi.org/10.1016/j.hydromet.2008.01.006.

[44] J.K. H. Park, H. Lee, A processing for recycling of the domestic aluminum dross, in: Glob. Symp. Recycl. Waste Treat. Clean Technol. Vol. II. REWAS, San Sebastian, Spain, 1999: p. 995.

[45] E.A. El-Katatny, S.A. Halawy, M.A. Mohamed, M.I. Zaki, Surface composition, charge and texture of active alumina powders recovered from aluminum dross tailings chemical waste, Powder Technol. 132 (2-3) (2003) 137–144, https://doi.org/10.1016/S0032-5910(03)00047-0.

[46] A. López-Delgado, F.A. López, L. Gonzalo-Delgado, S. López-Andrés, F.J. Alguacil, Study by DTA/TG of the formation of calcium aluminate obtained from an aluminium hazardous waste, J. Therm. Anal. Calorim. 99 (3) (2010) 999–1004, https://doi.org/10.1007/s10973-009-0597-z.

[47] A. López-Delgado, H. Tayibi, C. Pérez, F.J. Alguacil, F.A. López, A hazardous waste from secondary aluminium metallurgy as a new raw material for calcium aluminate glasses, J. Hazard. Mater. 165 (1-3) (2009) 180–186, https://doi.org/10.1016/j.jhazmat.2008.09.124.

[48] E.M.M. Ewais, N.M. Khalil, M.S. Amin, Y.M.Z. Ahmed, M.A. Barakat, Utilization of aluminum sludge and aluminum slag (dross) for the manufacture of calcium aluminate cement, Ceram. Int. - CERAM INT. 35 (8) (2009) 3381–3388, https://doi.org/10.1016/j.ceramint.2009.06.008.

[49] A. Gil, E. Arrieta, M.A. Vicente, S.A. Korili, Synthesis and CO_2 adsorption properties of hydrotalcite-like compounds prepared from aluminum saline slag wastes, Chem. Eng. J. 334 (2018) 1341–1350, https://doi.org/10.1016/j.cej.2017.11.100.

[50] R. Galindo, A. López-Delgado, I. Padilla, M. Yates, Synthesis and characterisation of hydrotalcites produced by an aluminium hazardous waste: A comparison between the use of ammonia and the use of triethanolamine, Appl. Clay Sci. 115 (2015) 115–123, https://doi.org/10.1016/j.clay.2015.07.032.

[51] R. Galindo, A. López-Delgado, I. Padilla, M. Yates, Hydrotalcite-like compounds: A way to recover a hazardous waste in the aluminium tertiary industry, Appl. Clay Sci. 95 (2014) 41–49, https://doi.org/10.1016/j.clay.2014.03.022.

[52] L. Santamaría, M. López-Aizpún, M. García-Padial, M.A. Vicente, S.A. Korili, A. Gil, Zn-Ti-Al layered double hydroxides synthesized from aluminum saline slag wastes as efficient drug adsorbents, Appl. Clay Sci. 187 (2020) 105486, https://doi.org/10.1016/j.clay.2020.105486.

[53] L. Santamaria, F. Devred, E.M. Gaigneaux, M.A. Vicente, S.A. Korili, A. Gil, Effect of the surface properties of Me2+/Al layered double hydroxides synthesized from aluminium saline slag wastes on the adsorption removal of drugs, Micropor. Mesopor. Mater. 309 (2020), 110560, https://doi.org/10.1016/j.micromeso.2020.110560.

[54] L. Santamaría, M.A. Vicente, S.A. Korili, A. Gil, Saline slag waste as an aluminum source for the synthesis of Zn-Al-Fe-Ti layered double-hydroxides as catalysts for the photodegradation of emerging contaminants, J. Alloys Comp. 843 (2020) 156007, https://doi.org/10.1016/j.jallcom.2020.156007.

[55] J. Kim, K. Biswas, K.-W. Jhon, S.-Y. Jeong, W.-S. Ahn, Synthesis of $AlPO_4$-5 and $CrAPO^{-5}$ using aluminum dross, J. Hazard. Mater. 169 (1-3) (2009) 919–925, https://doi.org/10.1016/j.jhazmat.2009.04.035.

[56] N. Murayama, N. Okajima, S. Yamaoka, H. Yamamoto, J. Shibata, Hydrothermal synthesis of $AlPO_4$-5 type zeolitic materials by using aluminum dross as a raw material, J. Eur. Ceram. Soc. 26 (4-5) (2006) 459–462, https://doi.org/10.1016/j.jeurceramsoc.2005.06.022.

[57] S. Kuroki, T. Hashishin, T. Morikawa, K. Yamashita, M. Matsuda, Selective synthesis of zeolites A and X from two industrial wastes: Crushed stone powder and aluminum ash, J. Environ. Manage. 231 (2019) 749–756, https://doi.org/10.1016/j.jenvman.2018.10.082.

[58] C. Belviso, A. Kharchenko, E. Agostinelli, F. Cavalcante, D. Peddis, G. Varvaro, N. Yaacoub, S. Mintova, Red mud as aluminium source for the synthesis of magnetic zeolite, Microporous Mesoporous Mater. 270 (2018) 24–29, https://doi.org/10.1016/j.micromeso.2018.04.038.

[59] R. Sánchez-Hernández, A. López-Delgado, I. Padilla, R. Galindo, S. López-Andrés, One-step synthesis of NaP1, SOD and ANA from a hazardous aluminum solid waste, Microporous Mesoporous Mater. 226 (2016) 267–277, https://doi.org/10.1016/j.micromeso.2016.01.037.

[60] T. Hiraki, A. Nosaka, N. Okinaka, T. Akiyama, Synthesis of zeolite-X from waste metals, ISIJ Int. 49 (10) (2009) 1644–1648, https://doi.org/10.2355/isijinternational.49.1644.

[61] M. Yoldi, E.G. Fuentes-Ordoñez, S.A. Korili, A. Gil, Zeolite synthesis from aluminum saline slag waste, Powder Technol. 366 (2020) 175–184, https://doi.org/10.1016/j.powtec.2020.02.069.

[62] A. Jiménez, A. Misol, A. Morato, V. Rives, M.A. Vicente, A. Gil, Synthesis of pollucite and analcine zeolites by recovering aluminium from a saline slag, J. Clean. Prod. 297 (2021), 126667, https://doi.org/10.1016/j.jclepro.2021.126667.

[63] Y. Cardona, S.A. Korili, A. Gil, A nonconventional aluminum source in the production of alumina-pillared clays for the removal of organic pollutants by adsorption, Chem. Eng. J. 425 (2021) 130708, https://doi.org/10.1016/j.cej.2021.130708.

[64] J.J. Torrez-Herrera, E.G. Fuentes-Ordoñez, S.A. Korili, A. Gil, Evidence for the synthesis of La-hexaaluminate from aluminum-containing saline slag wastes: Correction of structural defects and phase purification at low temperature, Powder Technol. 377 (2021) 80–88, https://doi.org/10.1016/j.powtec.2020.08.087.

[65] J.J. Torrez-Herrera, S.A. Korili, A. Gil, Structure and activity of nickel supported on hibonite-type La-hexaaluminates synthesized from aluminum saline slags for the dry reforming of methane, Chem. Eng. J. Adv. 5 (2021) 100080, https://doi.org/10.1016/j.ceja.2020.100080.

[66] T.H. Gardner, J.J. Spivey, E.L. Kugler, A. Campos, J.C. Hissam, A.D. Roy, Structural characterization of Ni-substituted hexaaluminate catalysts using EXAFS, XANES, XPS, XRD, and TPR, J. Phys. Chem. C. 114 (17) (2010) 7888–7894, https://doi.org/10.1021/jp9117634.

[67] J.M. Rynkowski, T. Paryjczak, M. Lenik, On the nature of oxidic nickel phases in NiO/γ-Al_2O_3 catalysts, Appl. Catal. A, Gen. 106 (1) (1993) 73–82, https://doi.org/10.1016/0926-860X(93)80156-K.

[68] J. Gao, C. Jia, J. Li, M. Zhang, F. Gu, G. Xu, Z. Zhong, F. Su, Ni/Al_2O_3 catalysts for CO methanation: Effect of Al_2O_3 supports calcined at different temperatures, J. Energy Chem. 22 (6) (2013) 919–927, https://doi.org/10.1016/S2095-4956(14)60273-4.

[69] J. Zhang, H. Xu, X. Jin, Q. Ge, W. Li, Characterizations and activities of the nano-sized Ni/Al_2O_3 and Ni/La-Al_2O_3 catalysts for NH_3 decomposition, Appl. Catal. A Gen. 290 (1-2) (2005) 87–96, https://doi.org/10.1016/j.apcata.2005.05.020.

[70] A.N. Pinheiro, A. Valentini, José.M. Sasaki, A.C. Oliveira, Highly stable dealuminated zeolite support for the production of hydrogen by dry reforming of methane, Appl. Catal. A Gen. 355 (1-2) (2009) 156–168, https://doi.org/10.1016/j.apcata.2008.12.007.

[71] S. Damyanova, B. Pawelec, K. Arishtirova, J.L.G. Fierro, C. Sener, T. Dogu, MCM-41 supported PdNi catalysts for dry reforming of methane, Appl. Catal. B Environ. 92 (3-4) (2009) 250–261, https://doi.org/10.1016/j.apcatb.2009.07.032.

[72] D.G. Araiza, D.G. Arcos, A. Gómez-Cortés, G. Díaz, Dry reforming of methane over Pt-Ni/CeO_2 catalysts: Effect of the metal composition on the stability, Catal. Today 360 (2021) 46–54, https://doi.org/10.1016/j.cattod.2019.06.018.

[73] J.J. Torrez-Herrera, S.A. Korili, A. Gil, Effect of the synthesis method on the morphology, textural properties and catalytic performance of La-hexaaluminates in the dry reforming of methane, J. Environ. Chem. Eng. 9 (2021), 105298, https://doi.org/10.1016/j.jece.2021.105298.

[74] G. Jiang, X. Zhang, F. Zhang, Z. Liu, Z. Wang, Z. Hao, C. Lin, Efficient recovery of hydrogen and sulfur resources over non-sulfide based $LaFe_xAl_{12-x}O_{19}$ hexaaluminate catalysts by H_2S catalytic decomposition, Appl. Catal. B Environ. 263 (2020), 118354, https://doi.org/10.1016/j.apcatb.2019.118354.

[75] N.M. Alawi, A. Barifcani, H.R. Abid, Optimisation of CH_4 and CO_2 conversion and selectivity of H_2 and CO for the dry reforming of methane by a microwave plasma technique using a Box-Behnken design, Asia-Pacific J. Chem. Eng. 13 (2018) e2254, https://doi.org/10.1002/apj.2254.

[76] P. Cao, S. Adegbite, H. Zhao, E. Lester, T. Wu, Tuning dry reforming of methane for F-T syntheses: A thermodynamic approach, Appl. Energy. 227 (2018) 190–197, https://doi.org/10.1016/j.apenergy.2017.08.007.

[77] F.A.J. Al-Doghachi, A. Islam, Z. Zainal, M.I. Saiman, Z. Embong, Y.H. Taufiq-Yap, G. Yang, High coke-resistance Pt/$Mg_{1-x}Ni_xO$ catalyst for dry reforming of methane, Plos One 11 (1) (2016) e0145862, https://doi.org/10.1371/journal.pone.014586210.1371/journal.pone.0145862.g00110.1371/journal.pone.0145862.g00210.1371/journal.pone.0145862.g00310.1371/journal.pone.0145862.g00410.1371/journal.pone.0145862.g00510.1371/journal.pone.0145862.g00610.1371/journal.pone.0145862.g00710.1371/journal.pone.0145862.g00810.1371/journal.pone.0145862.g00910.1371/journal.pone.0145862.g01010.1371/journal.pone.0145862.g01110.1371/journal.pone.0145862.g01210.1371/journal.pone.0145862.g01310.1371/journal.pone.0145862.g01410.1371/journal.pone.0145862.g01510.1371/journal.pone.0145862.g01610.1371/journal.pone.0145862.t00110.1371/journal.pone.0145862.t00210.1371/journal.pone.0145862.s001.

[78] A. Wolfbeisser, O. Sophiphun, J. Bernardi, J. Wittayakun, K. Föttinger, G. Rupprechter, Methane dry reforming over ceria-zirconia supported Ni catalysts, Catal. Today 277 (2016) 234–245, https://doi.org/10.1016/j.cattod.2016.04.025.

[79] C.P.B. Quitete, R.C.P. Bittencourt, M.M.V.M. Souza, Steam reforming of tar using toluene as a model compound with nickel catalysts supported on hexaaluminates, Appl. Catal. A Gen. 478 (2014) 234–240, https://doi.org/10.1016/j.apcata.2014.04.019.

[80] E. le Saché, S. Johnson, L. Pastor-Pérez, B. Amini Horri, T. Reina, Biogas upgrading via dry reforming over a Ni-Sn/CeO_2-Al_2O_3 catalyst: influence of the biogas source, Energies 12 (6) (2019) 1007, https://doi.org/10.3390/en12061007.

[81] L. Foppa, M.-C. Silaghi, K. Larmier, A. Comas-Vives, Intrinsic reactivity of Ni, Pd and Pt surfaces in dry reforming and competitive reactions: Insights from first principles calculations and microkinetic modeling simulations, J. Catal. 343 (2016) 196–207, https://doi.org/10.1016/j.jcat.2016.02.030.

[82] K. Nagaoka, K. Seshan, K.-ichi. Aika, J.A. Lercher, Carbon deposition during carbon dioxide reforming of methane-comparison between Pt/Al_2O_3 and Pt/ZrO_2, J. Catal. 197 (1) (2001) 34–42, https://doi.org/10.1006/jcat.2000.3062.

[83] D. Li, Y. Nakagawa, K. Tomishige, Methane reforming to synthesis gas over Ni catalysts modified with noble metals, Appl. Catal. A Gen. 408 (1-2) (2011) 1–24, https://doi.org/10.1016/j.apcata.2011.09.018.

[84] J. Guo, C. Xie, K. Lee, N. Guo, J.T. Miller, M.J. Janik, C. Song, Improving the carbon resistance of Ni-based steam reforming catalyst by alloying with Rh: a computational study coupled with reforming experiments and EXAFS Characterization, ACS Catal. 1 (6) (2011) 574–582, https://doi.org/10.1021/cs2000472.

[85] V. Dal Santo, A. Gallo, A. Naldoni, M. Guidotti, R. Psaro, Bimetallic heterogeneous catalysts for hydrogen production, Catal. Today 197 (1) (2012) 190–205, https://doi.org/10.1016/j.cattod.2012.07.037.